



HAL
open science

Simulating Longitudinal Brain MRIs with known Volume Changes and Realistic Variations in Image Intensity

Bishesh Khanal, Nicholas Ayache, Xavier Pennec

► **To cite this version:**

Bishesh Khanal, Nicholas Ayache, Xavier Pennec. Simulating Longitudinal Brain MRIs with known Volume Changes and Realistic Variations in Image Intensity. *Frontiers in Neuroscience*, 2017, 10.3389/fnins.2017.00132 . hal-01348959v2

HAL Id: hal-01348959

<https://inria.hal.science/hal-01348959v2>

Submitted on 7 Feb 2017 (v2), last revised 22 Mar 2017 (v3)

HAL is a multi-disciplinary open access archive for the deposit and dissemination of scientific research documents, whether they are published or not. The documents may come from teaching and research institutions in France or abroad, or from public or private research centers.

L'archive ouverte pluridisciplinaire **HAL**, est destinée au dépôt et à la diffusion de documents scientifiques de niveau recherche, publiés ou non, émanant des établissements d'enseignement et de recherche français ou étrangers, des laboratoires publics ou privés.

Simulating Longitudinal Brain MRIs with known Volume Changes and Realistic Variations in Image Intensity

Bishesh Khanal, Nicholas Ayache, and Xavier Pennec

Asclepios, INRIA Sophia Antipolis Méditerranée, Sophia Antipolis, France

Correspondence*:

Bishesh Khanal

bishesh.khanal@inria.fr

2 ABSTRACT

3 This paper presents a simulator tool that can simulate large databases of visually realistic
4 longitudinal MRIs with known volume changes. The simulator is based on a previously proposed
5 biophysical model of brain deformation due to atrophy in AD. In this work, we propose a novel
6 way of reproducing realistic intensity variation in longitudinal brain MRIs, which is inspired by an
7 approach used for the generation of synthetic cardiac sequence images. This approach combines
8 a deformation field obtained from the biophysical model with a deformation field obtained by a
9 non-rigid registration of two images. The combined deformation field is then used to simulate a
10 new image with specified atrophy from the first image, but with the intensity characteristics of the
11 second image. This allows to generate the realistic variations present in real longitudinal time-
12 series of images, such as the independence of noise between two acquisitions and the potential
13 presence of variable acquisition artifacts. Various options available in the simulator software are
14 briefly explained in this paper. In addition, the software is released as an open-source repository.
15 The availability of the software allows researchers to produce tailored databases of images with
16 ground truth volume changes; we believe this will help developing more robust brain morphometry
17 tools. Additionally, we believe that the scientific community can also use the software to further
18 experiment with the proposed model, and add more complex models of brain deformation and
19 atrophy generation.

20 **Keywords:** Neurodegeneration, biophysical modelling, biomechanical simulation, simulated database, synthetic images, synthetic
21 longitudinal MRIs

1 INTRODUCTION

22 Structural Magnetic Resonance Imaging (MRI) has been widely used for in-vivo observation of
23 morphological changes over time in human brain. Atrophy or tissue volume loss measure from structural
24 MRI is an established biomarker for neurodegeneration (Frisoni et al., 2010). There is a large number of
25 brain morphometry algorithms developed in the literature which estimate global or local atrophy from
26 structural MRIs (Wright et al., 1995; Freeborough and Fox, 1997; Ashburner and Friston, 2000; Smith et al.,

27 2002; Hua et al., 2008). Volume/atrophy measurements obtained from such algorithms have been used to
28 test various clinical hypotheses about neurodegenerative diseases (Wright et al., 1995; Sepulcre et al., 2006;
29 Koch et al., 2016). Similarly, comparison of different neurodegenerative diseases have also been performed
30 based on these measurements (Rosen et al., 2002; Whitwell and Jack Jr, 2005). Since atrophy estimation is
31 an inverse problem, the estimation algorithms require a model with certain parameters. The results obtained
32 from such algorithms depend on model assumptions and the parameters used. Often, these assumptions
33 are implicit and cannot be directly linked to the biophysical process of neurodegeneration. For instance,
34 tensor based morphometry (TBM) encodes local volume changes by computing Jacobian determinants of
35 the deformation field obtained from non-linear registration of longitudinal MRIs (Ashburner and Ridgway,
36 2015). Such methods contain model biases because TBM results depend on the choices of regularization
37 used during the registration of images (Ashburner, 2013). Likewise, edge-based methods such as BSI,
38 SIENA etc. are sensitive to unmatched image contrasts between scans, poor signal-to-noise ratio, partial
39 volume effects, segmentation errors etc. (Preboske et al., 2006; Prados et al., 2015). Estimating and
40 correcting the bias present in such morphometry tools is important, especially for clinical applications.

41 In addition to tracking volumetric changes in specific brain structures, longitudinal imaging data can also
42 be used to study the temporal inter-relationship of atrophy in different structures. For instance, Carmichael
43 et al. (2013) studied the groupings of 34 cortical regions and hippocampi from the per-individual rates of
44 atrophy estimates in these regions. In Fonteijn et al. (2012), authors defined AD progression as a series
45 of discrete events. Along with other clinical events, the timings of atrophy in various brain structures
46 were included in a set of discrete events. Without any prior to their ordering, the model finds the most
47 probable order for these events from the data itself. They used Bayesian statistical algorithms for fitting the
48 event-based disease progression model. The objective of these studies were to understand how different
49 regions of brain evolve during the neurodegeneration.

50 In this context of increasing use of the atrophy measurements from longitudinal MRIs in testing or
51 discovering clinically relevant hypotheses, it is important to study the bias and variability of the atrophy
52 estimation algorithms. The actual volume changes in real longitudinal MRIs are not known. Thus, the
53 evaluation and validation of atrophy estimation algorithms require generating images with known volume
54 changes, called ground truth images.

55 A number of atrophy simulators have been proposed in the literature to produce ground truth MRIs
56 (Smith et al., 2003; Camara et al., 2006; Karaçali and Davatzikos, 2006; Pieperhoff et al., 2008; Sharma
57 et al., 2010; Modat et al., 2014; Radua et al., 2014; Khanal et al., 2016b). Most of these simulators use a
58 model that attempts to produce a deformation field with the specified volume changes in the input brain
59 MRI. To produce realistic scenarios of noise and acquisition artifacts, some of these simulators also use a
60 model to produce noise and artifacts in the simulated image.

61 Such simulators have been used for the validation of registration or segmentation based atrophy estimation
62 algorithms (Camara et al., 2008; Pieperhoff et al., 2008; Sharma et al., 2010), to estimate the bias in such
63 algorithms, and also to estimate uncertainty in the measured atrophy (Sharma et al., 2013). These studies
64 have estimated the bias by simulating simple atrophy patterns in a small number of brain regions, or
65 uniform diffused global atrophies. However, real case scenarios could have a much more complex atrophy
66 distribution occurring in many brain structures at the same time.

67 Noise and imaging artifacts have an important impact on the results obtained from atrophy estimation
68 algorithms (Pieperhoff et al., 2008; Camara et al., 2008; Sharma et al., 2010). Thus, proper evaluation
69 of atrophy estimation algorithms by using simulated ground truth images requires simulation of realistic

70 variation in noise and intensity too. All the previous atrophy simulators have warped the input baseline
71 image with the deformation field obtained from a model of brain deformation. Then, extra noise and
72 artifacts are added on this warped image by using another artificial model. The intensity noise in structural
73 MRIs has been shown to be governed by a Rician distribution where the noise is Gaussian in k-space
74 (Gudbjartsson and Patz, 1995). Thus the Rician noise can be added in the simulated images as follows:

- 75 • Use two independent random variables following zero-mean Gaussian distribution to compute the real
76 and imaginary parts of a complex number at each voxel.
- 77 • Considering the original intensity to be a complex number with zero imaginary part, add the real and
78 imaginary components obtained above and take the magnitude of the resulting complex signal.

79 For example, Sled et al. (1998) used this approach to add noise in simulated MRIs that were used for
80 the validation of intensity bias correction scheme they presented. Using the same approach, Camara et al.
81 (2008) added noise to the simulated ground truth images with atrophy.

82 In addition to the Rician noise described above, other noise and artifacts are also present in MRIs
83 (Simmons et al., 1994). Some of the artifact sources that have been shown to affect the measurements of
84 atrophy estimation algorithms (Camara-Rey et al., 2006; Sharma et al., 2010; Pieperhoff et al., 2008) are:

- 85 • Bias field inhomogeneity arising due to poor radio frequency (RF) coil uniformity.
- 86 • Geometrical distortions that are present due to the errors in gradient field strength and non-linearity of
87 gradient fields in the MR scanner (Langlois et al., 1999).
- 88 • Interpolation of intensities during various pre-processing steps of TBM based analysis framework (e.g.,
89 resampling of the images into a common template space).

90 Many other acquisition artifacts may not be simulated because we do not have faithful models. Inability to
91 produce realistic intensity variation and noise in simulated longitudinal images is one of the key limitations
92 in the state-of-the-art atrophy simulators, including our previous work (Khanal et al., 2016b). In this work,
93 we propose a simple but elegant solution to remove the limitation of previous atrophy simulators. First, our
94 biophysical model of brain deformation (Khanal et al., 2016b) is used to obtain a dense deformation field
95 with specified volume changes. Then, to obtain realistic intensity variations, intensities in the simulated
96 images are resampled from baseline repeat scans of the same patient. Although the method is very simple
97 and straightforward, this allows simulating longitudinal images with variation in intensity and noise taken
98 from real scans themselves without explicitly specifying any noise or artifact models. To the best of our
99 knowledge, this idea was not presented before in the literature. When the repeat scans are not available,
100 we use an approach introduced by Prakosa et al. (2013) where the authors simulate visually realistic time
101 series of cardiac images. Intensity variation in the simulated images of a patient is obtained by resampling
102 the intensities from the repeat scans if available, otherwise from the real images of the same patient taken
103 at different times.

104 Figure 1 shows a diagram of the complete framework. To implement this framework, we have developed
105 an open-source atrophy simulator software called `Simul@tropy`¹. To our knowledge, `Simul@tropy`
106 is the first atrophy simulator to be made open-source. `Simul@tropy` uses the biophysical model
107 presented in Khanal et al. (2016b) but introduces a new numerical scheme to compute divergence, which
108 removes the numerical inconsistency presented in the previous work. This is further explained in detail in
109 Section 4.2.

¹ Available at <https://inria-asclepios.github.io/simul-atropy/>

110 Section 2 explains all the blocks of the framework shown in Figure 1. Starting from a small set of real
 111 scans, we show how longitudinal images with different atrophy patterns and realistic intensity variations
 112 can be simulated. Section 3 shows some simulation results using `Simul@trophy`, and also illustrates
 113 some potential applications of the simulator. In Section 4, we present some example simulations to illustrate
 114 some of the important points to consider when using `Simul@trophy` for different applications, such as
 115 evaluation of atrophy estimation algorithms, validation of data-driven disease progression models, training
 116 of brain morphometry algorithms based on machine learning etc.

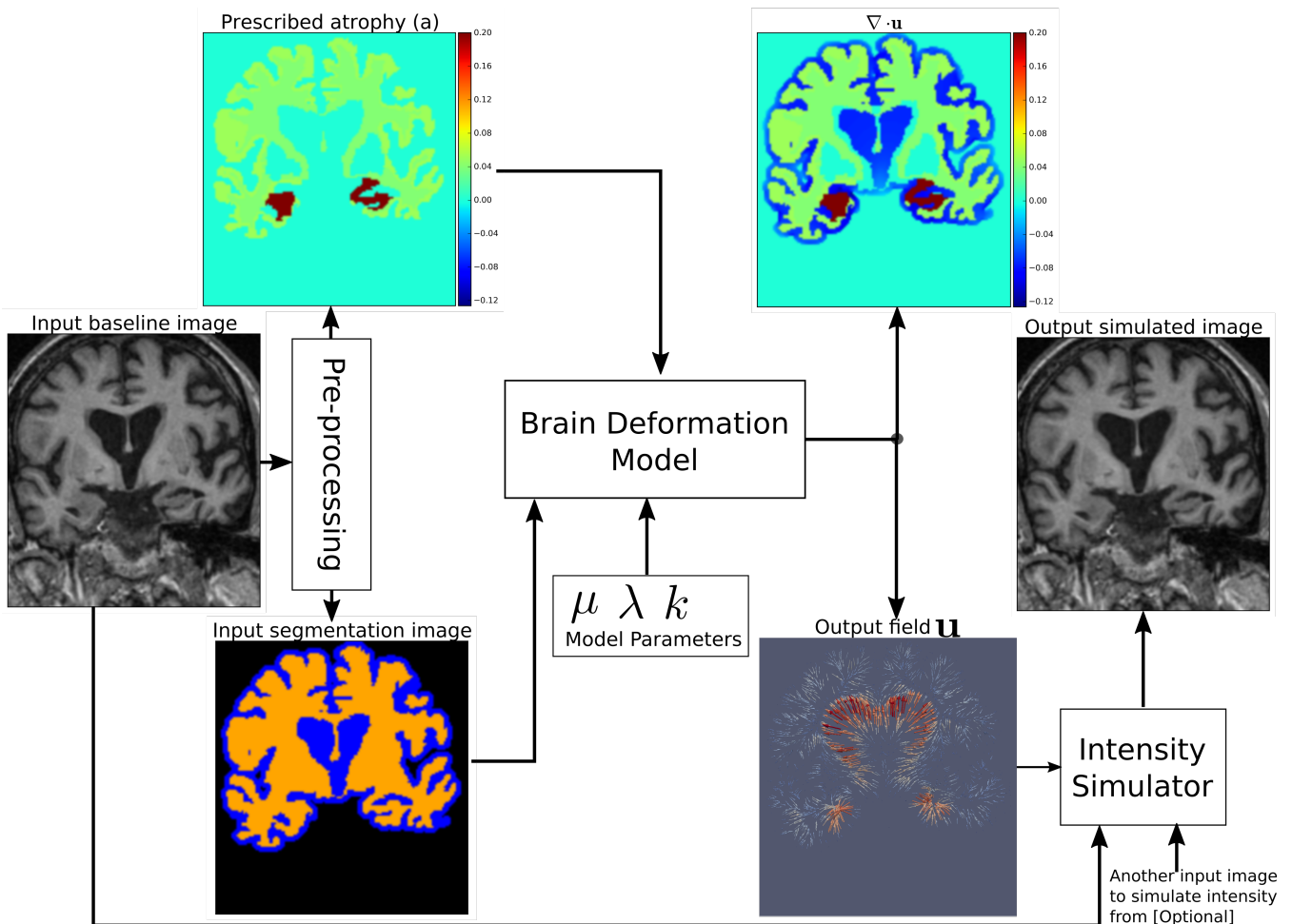


Figure 1. Pipeline to simulate synthetic images using `Simul@trophy`. Starting from a real baseline image of a subject, synthetic images with known volume changes can be generated. These synthetic images can follow intensity characteristics of either the input baseline or other images of the same subject. Pre-processing is required to generate an atrophy map and a segmentation image, which are fed as inputs to the brain deformation model. For a given set of parameters, the model computes a velocity field whose divergence is equal to the prescribed atrophy map at each voxel of the regions selected by using the segmentation image. Intensity simulator uses the output field to produce synthetic image whose intensity is resampled either from the input real baseline or from any other image as desired.

2 SIMULATING REALISTIC LONGITUDINAL IMAGES WITH ATROPHY/GROWTH

117 We use the biophysical model presented in Khanal et al. (2014, 2016b) to generate dense deformation field
 118 with specified complex patterns of volume changes. This deformation field is then used to generate realistic

119 synthetic longitudinal images with intensity variation, noise and artifacts, just like in real longitudinal
120 images. The major components of the simulation framework, as seen in Figure 1, are: i) Pre-processing ii)
121 Brain deformation model iii) Realistic intensity simulator.

122 2.1 Pre-processing to generate a segmentation image and atrophy maps

123 A pre-processing step takes a real scan of a patient as an input baseline image, and generates the required
124 inputs of the brain deformation model: a segmentation image and a specified atrophy map.

125 2.1.1 Segmentation image

126 There are three labels in the segmentation image used by `Simul@tropy` (Figure 1):

- 127 • `Label0`: regions where no deformation should be prescribed,
- 128 • `Label1`: regions where the deformation model is allowed to adapt volume changes as required,
- 129 • `Label2`: regions where certain volume changes are prescribed (the values of volume changes are
130 provided with an input atrophy map).

131 Pre-processing usually starts with a brain extraction that excludes the skull and outside regions (also
132 called skull stripping). Skull stripping is followed by a segmentation such that each voxel of the input
133 image could be assigned to one of the three labels. For example, a typical pre-processing step that includes
134 a segmentation of brain parenchyma and CSF would produce a segmentation image with the following
135 labels:

- 136 • `Label0`: Skull and outside regions of the input image
- 137 • `Label1`: CSF regions
- 138 • `Label2`: Gray and white matter regions

139 2.1.2 Atrophy map

140 An atrophy map is a scalar image with desired values of volume changes in `Label1` regions of the
141 segmentation image, and zeros in all the other regions. It is defined at each voxel as follows:

$$a = \frac{V_0 - V_1}{V_0},$$

142 where V_0 and V_1 are the volumes of the material lying in a voxel at time t_0 and t_1 respectively. Thus,
143 regions with volume loss have positive values of a while the regions with volume expansion have negative
144 values of a . An example atrophy map is shown in Figure 1. In this work, we illustrate example simulations
145 where two kinds of pre-processing steps were used to generate the atrophy maps:

146 Segmentation based atrophy map

147 The user can set uniform values of atrophy in regions of interests (ROIs) of the brain. In this case, one
148 must first perform a segmentation of all ROIs in which a non-zero value of atrophy is desired. Then, it
149 is straightforward to create a scalar image having intensity values taken from a table, which contains the
150 labels of ROIs and the corresponding desired atrophy values.

151 Registration based atrophy map

152 The results of longitudinal non-rigid registration can be used to estimate local volume changes, for instance
153 by computing Jacobian determinants of the displacement fields or by computing the divergence of the

154 stationary velocity fields obtained from the registration. These local volume changes obtained from the
 155 registration based methods are usually smoothly varying in space and can be used to prescribe either:

- 156 • smoothly varying atrophy maps,
- 157 • or atrophy maps uniform in ROIs obtained by averaging, in each ROIs, the atrophy obtained above.

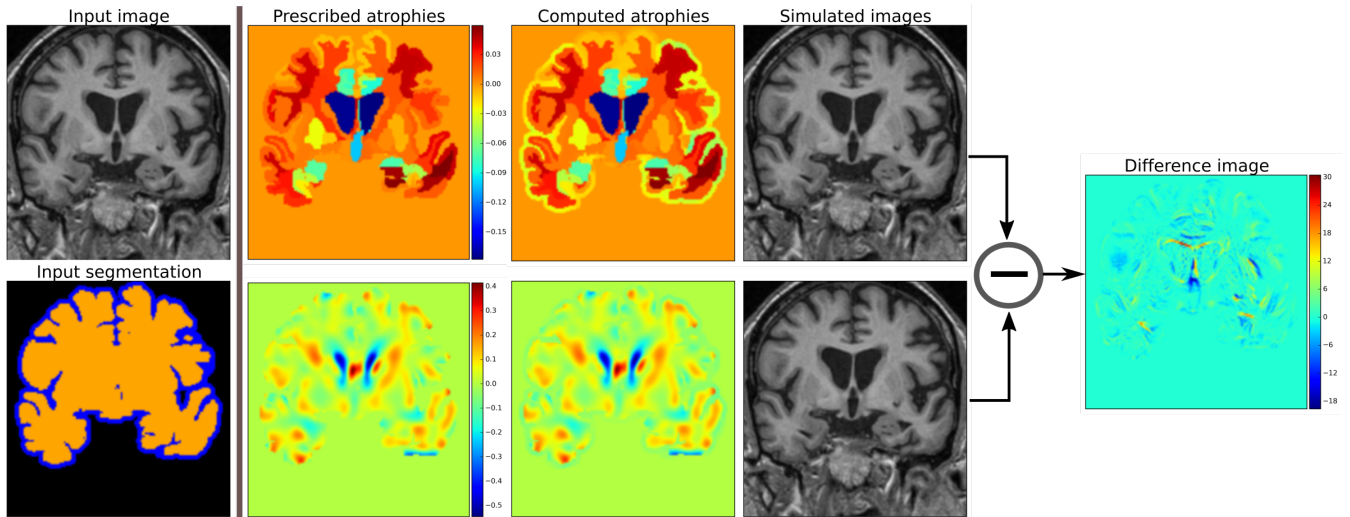


Figure 2. Examples of two different kinds of atrophy maps. The first row prescribes an atrophy map that is uniform in different regions of the brain, while the second row prescribes a smoothly varying atrophy. Both of these atrophy maps have same average values in each ROIs. The example also shows that we can prescribe volume changes in ventricles, if desired, by adapting the input segmentation map accordingly. The simulated images, as shown, are different although they have same mean regional atrophy values. The prescribed atrophy maps and the corresponding computed atrophy maps have different values of atrophy in the regions with sulcal CSF because it is part of `Label1` (blue color in the segmentation map) where the volume is allowed to freely change.

158 Figure 2 shows two such atrophy maps with very different patterns, but having the same average regional
 159 volume changes.

160 2.2 A biophysical model of brain deformation with prescribed volume changes

161 `Simul@trophy` uses the biomechanics based model of brain deformation detailed in Khanal et al.
 162 (2016b). The model abstracts the phenomenon that evolves during several months or years in the brain at a
 163 macroscopic scale. It is based on the assumption that atrophy creates an internal stress which results in the
 164 deformation minimizing a strain energy. In other words, the brain parenchyma deforms with the prescribed
 165 atrophy by minimizing the strain energy. The strain energy corresponding to the prescribed atrophy at each
 166 time step is completely released when starting the next time step, which leads to a creep flow model.

167 For a given segmentation image, the model yields a deformation field with the prescribed atrophy at each
 168 voxel of `Label2` regions (e.g. brain parenchyma). `Label1` regions (e.g. the CSF) will correspondingly
 169 adapt its volume to globally compensate for the prescribed volume changes in the `Label2` regions. For
 170 a single time-step, the displacement field \mathbf{u} is obtained by solving the system of Eqs 1, where Dirichlet
 171 boundary conditions of zero deformation are prescribed in `Label0` regions.

$$\left. \begin{array}{l} \text{Regions with: Label10} \\ \mathbf{u} = 0 \\ \text{Dirichlet boundary conditions} \end{array} \right\} \quad \left. \begin{array}{l} \text{Label11} \\ \mu\Delta\mathbf{u} - \nabla p=0 \\ \nabla \cdot \mathbf{u} + kp=0 \end{array} \right\} \quad \left. \begin{array}{l} \text{Label12} \\ \mu\Delta\mathbf{u} - \nabla p=(\mu + \lambda)\nabla a \\ \nabla \cdot \mathbf{u} = -a \end{array} \right\} \quad (1)$$

172 The system of Eqs. 1 shows that the incompressibility constraint is relaxed in Label11 regions, while it
173 is strictly satisfied in Label12 regions.

174 The prescribed atrophy map a in the constraint $\nabla \cdot \mathbf{u} = -a$ is the amount of atrophy in a small time step
175 Δt such that the displacement field \mathbf{u} and its gradient are small enough to make the following approximation:
176 $\nabla \cdot \mathbf{u} = -a \approx J - 1$, where J is the Jacobian determinant (Khanal et al., 2016b). Jacobian determinant
177 measures the relative volume of a warped voxel, V_1/V_0 .

178 The impact of the choice of different values for the model parameters μ , λ and k are detailed in Khanal
179 et al. (2016b). For the same prescribed volume changes, we can obtain different deformation fields by
180 varying these model parameters. In this work, we focus on generating ground truth images with known
181 volume changes and not necessarily generating the exact evolution of the AD patients. Hence, we set the
182 model parameters as follows unless specified otherwise: $\mu = 1$ kPa, $\lambda = 0$ kPa, $k = 1$ kPa⁻¹.

183 Once the field \mathbf{u} with the prescribed volume changes is obtained from the model as described above by
184 using an input baseline image I_b , we can simulate a synthetic follow-up image I_s as follows:

- 185 • Let $\mathbf{y} = \Phi_{\text{sim}}(\mathbf{x}) = \mathbf{u} + \mathbf{x}$ describe a mapping of a point \mathbf{x} in physical space to another point \mathbf{y} by
186 applying the transformation corresponding to the dense deformation field Φ_{sim} , or the displacement
187 field \mathbf{u} .
- 188 • Let $\Phi_{\text{sim}} \star I_b$ describe an action of the diffeomorphism Φ_{sim} on the image I_b . Thus, the new synthetic
189 image I_s , obtained by warping I_b with the deformation field Φ_{sim} is given by:

$$I_s = \Phi_{\text{sim}} \star I_b = I_b \circ \Phi_{\text{sim}}^{-1}.$$

190 Figure 2 shows two simulated images from the same input baseline image but with two different atrophy
191 patterns.

192 2.3 Adding realistic intensity variation to synthetic longitudinal MRIs

193 In realistic scenarios, longitudinal MRIs are taken at multiple scan sessions often with slightly different
194 acquisition parameters or even with different scanners. For generating more realistic synthetic longitudinal
195 MRIs, variations in intensity and noise present in real longitudinal MRIs must also be simulated. If multiple
196 repeat scans of a subject are available, we can use them to simulate such variations in synthetic longitudinal
197 sequences. Assuming that all the available scans of the subject are already aligned using affine registration,
198 this section explains the proposed method of adding realistic variations in the intensity characteristics.

199 Starting from an input baseline image I_{b_0} of a subject, the previous sections explained how we can obtain
200 a deformation field Φ_{sim} from the brain deformation model, and use it to simulate a follow-up image

$$I_{s_0} = \Phi_{\text{sim}} \star I_{b_0}.$$

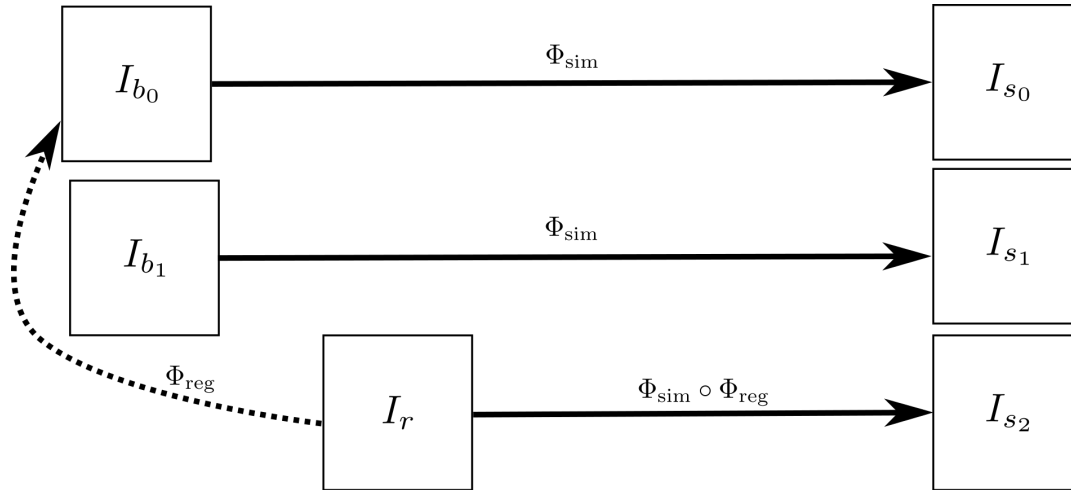


Figure 3. I_{b_0} and I_{b_1} are the repeat scans of a subject taken within a short period of time during which there is no morphological changes in the brain of the subject. I_r is taken at a later time when the brain could have undergone some morphological changes. The deformation field Φ_{reg} is obtained by registering I_r to I_{b_0} , while Φ_{sim} is obtained from the brain deformation model using I_{b_0} as the input image. The three simulated images I_{s_0} , I_{s_1} and I_{s_2} are all same time-point images but have different intensities that come from I_{b_0} , I_{b_1} and I_r respectively.

201 I_{s_0} has the same intensity characteristics as I_{b_0} , and the intensity noise in I_{s_0} is strongly correlated to the
 202 noise present in I_{b_0} .

203 If I_{b_1} is another scan of the same subject taken on the same day, we can obtain a new simulated image by
 204 resampling the intensity from I_{b_1} , but still using the same Φ_{sim} :

$$I_{s_1} = \Phi_{sim} \star I_{b_1}$$

205 The realistic variation of intensity and artifacts present between the two real scans I_{b_0} and I_{b_1} are now also
 206 present between the real baseline image I_{b_0} and the simulated follow-up image I_{s_1} .

207 The above approach assumes that the brain has not undergone any morphological changes between the
 208 scan sessions of the two real images. If the scan time-points of the two images are too far apart to have this
 209 assumption valid, we can no longer directly apply Φ_{sim} to the second image. Let I_r be another real scan of
 210 the patient taken at a time later than that of the baseline image I_{b_0} . There might be some morphological
 211 changes (e.g. atrophy) in I_r compared to I_{b_0} .

212 To simulate a new synthetic image with the same atrophy as that of I_{s_0} but with the intensity resampled
 213 from I_r , we must first perform a non-rigid registration between I_r and I_{b_0} . If Φ_{reg} is the deformation field
 214 obtained from the non-rigid registration between I_r and I_{b_0} , it can be used to get an image $\Phi_{reg} \star I_r$ which
 215 is aligned to I_{b_0} . In the ideal case, $\Phi_{reg} \star I_r$ and I_{b_0} are perfectly aligned with the only differences lying in
 216 the intensity characteristics and the noise.

217 We can now compose the deformation fields Φ_{sim} and Φ_{reg} to generate a new synthetic image as follows:

$$I_{s_2} = (\Phi_{sim} \circ \Phi_{reg}) \star I_r.$$

218 I_{s_2} has the same atrophy as that of I_{s_0} but with the intensity characteristics of I_r . Figure 3 illustrates how
 219 we obtain I_{s_0} , I_{s_1} and I_{s_2} . These three simulated images have the volume changes as encoded by Φ_{sim} , but
 220 have intensity characteristics coming from three different real images of the same patient.

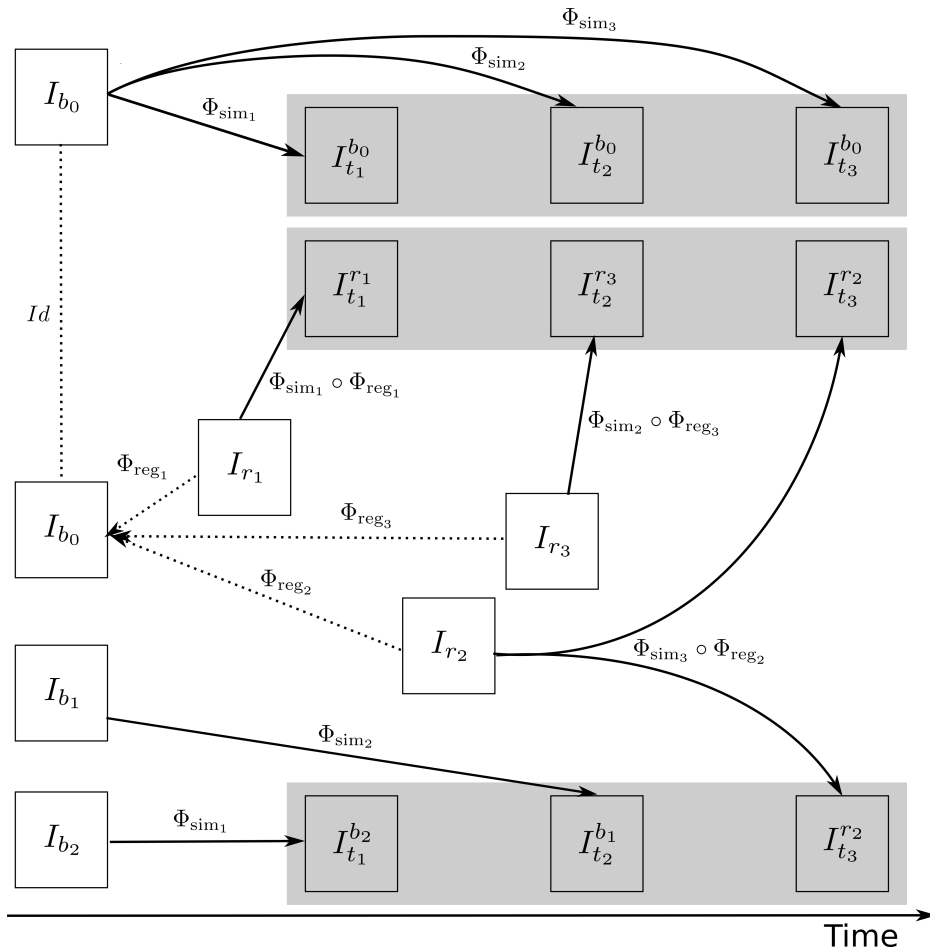


Figure 4. A general approach to simulate ground truth synthetic longitudinal images with realistic intensity variations; simulated images are shown within the shaded regions. The deformation fields with a prescribed atrophy for three time-points (Φ_{sim_1} , Φ_{sim_2} , and Φ_{sim_3}) are obtained from the biophysical model using I_{b_0} as the input baseline image. Several different sets of longitudinal images can then be simulated by resampling intensities from different combinations of available real images. The topmost shaded region shows a longitudinal sequence with no realistic intensity variations where the synthetic images are all resampled from I_{b_0} . The remaining two shaded regions have longitudinal sequences with realistic intensity variations where the simulated images are resampled from other available images of the same subject. In the ideal case, the three sets of longitudinal sequences have exactly the same morphological changes but with different variations in intensity characteristics.

221 Figure 4 illustrates how the approach described in this section can be used to generate multiple sets
 222 of longitudinal simulated sequences having identical morphological evolution but different variations of
 223 intensities. The three shaded regions in Figure 4 are the sets of longitudinal sequences with identical
 224 volume changes but with different variations of intensities.

3 SIMULATION EXAMPLES WITH SIMUL@TROPHY

225 This section presents simulation examples of synthetic longitudinal MRIs with prescribed atrophy patterns
 226 and realistic intensity variations². The real input MRIs used for the simulations presented in this section
 227 come from the database made available by Hadj-Hamou et al. (2016). The images had already undergone the
 228 `Pre-Processing and Position Correction` steps of the Longitudinal Log-Demons Framework
 229 (LLDF) detailed in Hadj-Hamou et al. (2016). Starting from the publicly available OASIS dataset (Marcus
 230 et al., 2010), the images in the database had undergone intensity inhomogeneity correction using `ANTs -`
 231 `N4BiasFieldCorrection` (Avants et al., 2011), and had been transported to a common space using
 232 affine registration with `FSL - FLIRT` (Jenkinson and Smith, 2001).

233 Since all the simulated images must undergo interpolation of intensities, numerical scheme used in
 234 the interpolation will have an impact on the intensity characteristics of the simulated images. In all the
 235 simulation examples that follows, intensities were resampled using B-spline interpolation of order 3.

236 Figure 5 shows a simulation example where uniform atrophy patterns are prescribed in the hippocampi,
 237 the gray matter (GM), and the white matter (WM) regions. The ventricles and sulcal CSF regions are
 238 allowed to expand as required to compensate for the volume loss in the brain parenchyma. The figure
 239 shows two simulated images whose intensities are resampled from two different images: i) the input
 240 baseline image I_b ii) another follow-up image of the same subject, I_r . The figure also shows intensity
 241 histograms of these two simulated images for a selected ROI. The selected ROI is a 2D WM region where
 242 the simulated images do not have a distinct morphological changes from I_b . Thus, the differences in the
 243 intensity histograms of I_b and the simulated images for this ROI is mostly due to the variation in intensity
 244 characteristics of the different images. We can see from the figure that the intensity characteristics of the
 245 simulated image resampled from I_b closely matches the intensity characteristics of I_b . And resampling the
 246 intensity from a different image I_r of the same subject allows simulating realistic variation of intensities.

247 To simulate multiple time-point images, the following approach can be used:

- 248 • Get \mathbf{u}_0 by solving the system of Eqs. (1) using the initial atrophy map a_0 and the initial segmentation
 249 image L_0 as input.
- 250 • For each time step $t = 1$ to n :
 - 251 • Warp a_{t-1} and L_0 using $\mathbf{u}_{t-1} \circ \mathbf{u}_{t-2} \dots \circ \mathbf{u}_0$ to get a_t and L_t respectively.
 - 252 • Solve for \mathbf{u}_t using a_t and L_t as input.

253 Once all the deformation fields Φ_{s_i} corresponding to \mathbf{u}_i for $i = 0, 1, \dots, n$ are obtained, these deformation
 254 fields can be used as shown in Figure 4 to simulate different sequences of longitudinal images. As time step
 255 gets larger, the segmentation map is warped with an increasingly bigger displacement field using nearest
 256 neighbor interpolation, which could result in numerical instabilities. As the atrophy map is also warped at
 257 each time step, the global atrophy rate prescribed in the beginning is not necessarily preserved during the
 258 intermediate time-steps.

259 In Figure 6, a simulation example of two longitudinal sequences each having three new time-point images
 260 is shown. Both sequences were simulated by prescribing a smoothly varying atrophy pattern. The smoothly
 261 varying atrophy pattern prescribed in this example is more complex than the simple pattern used in the
 262 previous example. In brain parenchyma regions, it is the negative of the divergence of a stationary velocity
 263 field obtained by performing LCC log-Demons registration (Lorenzi et al., 2013) of the input baseline

² The simulation results are made available at <http://neurovault.org/collections/AUKWWYBC/> (Gorgolewski et al., 2015).

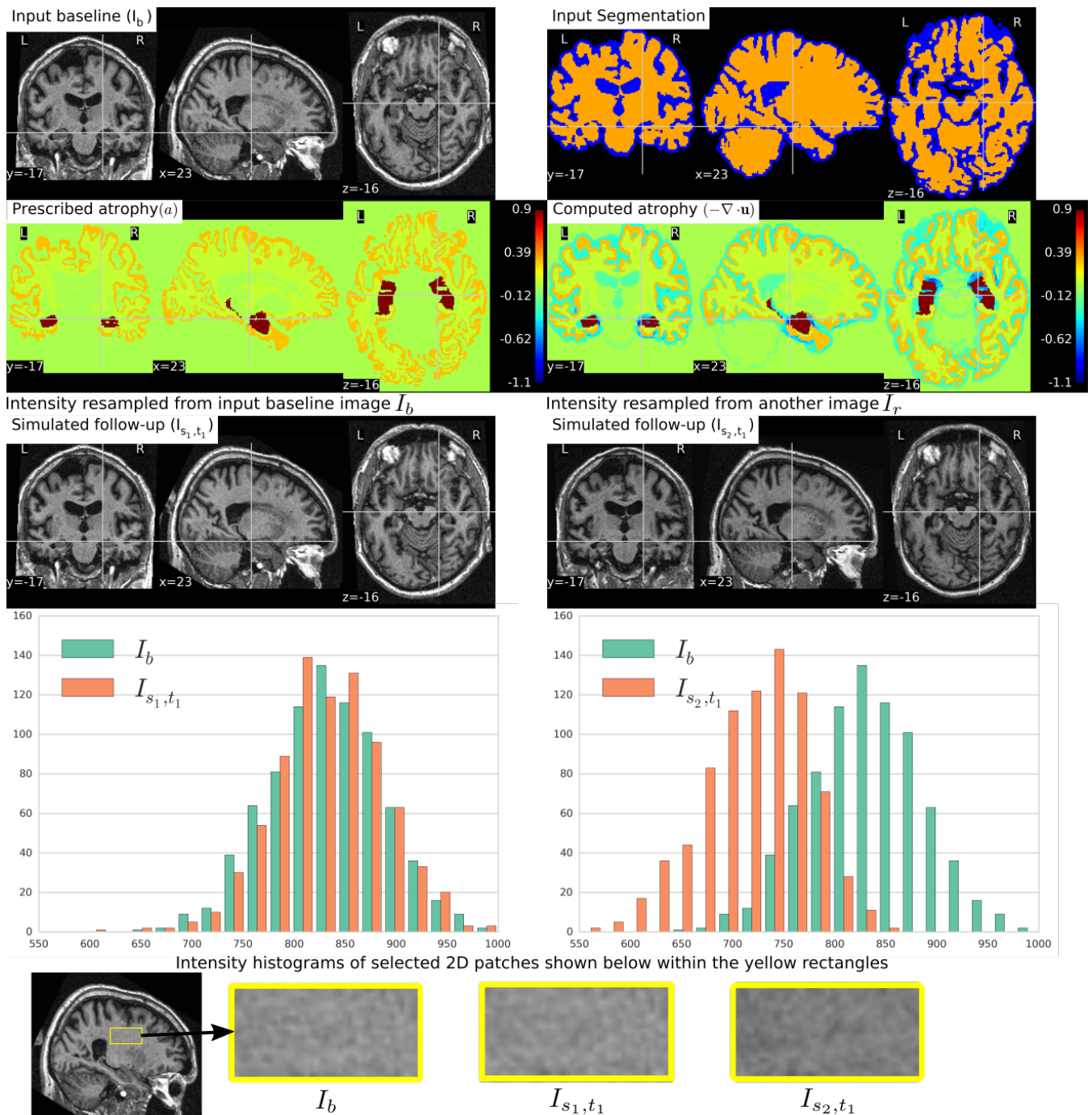


Figure 5. Two simulated images are shown on the third row where the image on the left is resampled from the input baseline image I_b , and the image on the right is resampled from another image I_r of the same subject. Both I_b and I_r had already been corrected for the bias field intensity inhomogeneity. The intensity histograms shown are of a selected ROI (shown on the last row) where there is no significant morphological changes between the images. From the histograms we can see that the simulated image I_{s_2, t_1} has a different intensity characteristics than I_b , while the simulated image I_{s_1, t_1} has intensity characteristics that closely matches to that of I_b .

264 image with a follow-up image of the same subject. The first sequence consists of all the images whose
 265 intensities are resampled from the same input baseline image I_b , while the second sequence consists of the
 266 images whose intensities are resampled from different real MRIs of the same subject. Thus, as shown in

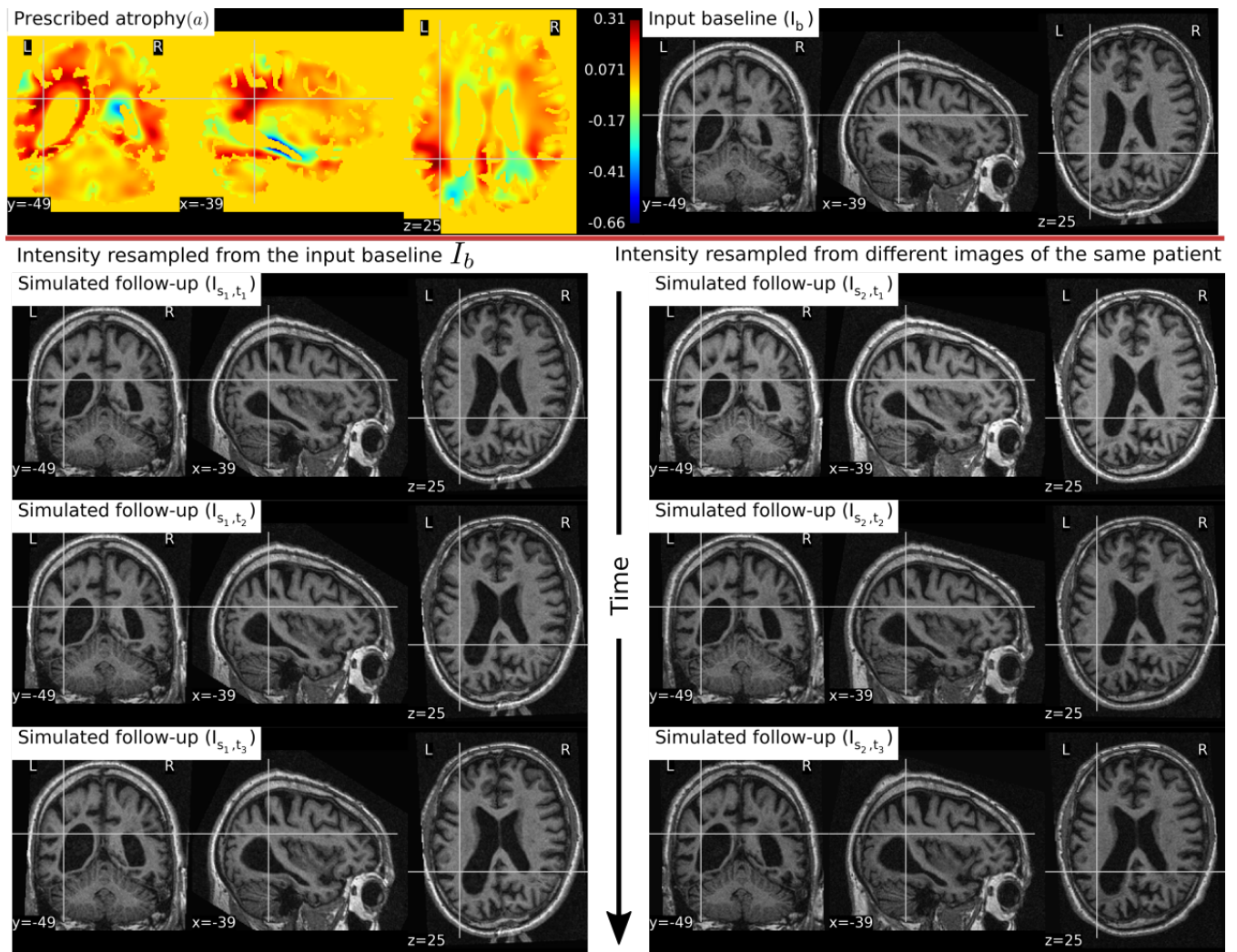


Figure 6. Two sets of synthetic longitudinal images are shown which are simulated by prescribing a smoothly varying atrophy pattern. The first row shows the input prescribed atrophy and the input baseline image I_b of a subject, while the remaining rows show the two sequences. The sequence shown on the left have simulated images that are all resampled from I_b . On the right, each simulated image is resampled from real MRIs of the same subject but taken at different times (at 0.68, 1.77 and 3.3 years after the baseline scan respectively). As shown by the intensity histograms of Figure 7, the longitudinal synthetic images on the right have more realistic intensity variations than the one left.

267 Figure 7, the first sequence does not have the realistic variation of intensities while the second sequence
 268 has the realistic variation of intensities. With this example, we also illustrated that we can generate multiple
 269 sequences of longitudinal images with same atrophy patterns but different variations of intensities.

270 Figure 8 shows a simulation example where we prescribe growth instead of atrophy in the brain tissue.
 271 The prescribed atrophy in this case is the negative of the atrophy map prescribed in Figure 6. From the
 272 segmentation image shown in Figure 8, we can see that the ventricles were allowed to adapt the volume
 273 changes as required to compensate for the volume changes in the brain parenchyma. From the three
 274 simulated time-points, we can see that these ventricles are shrinking and the brain parenchyma regions are
 275 expanding. The example shows that `Simul@tropy` can be used to simulate images of not only future
 276 time-points, but also the past time-point images.

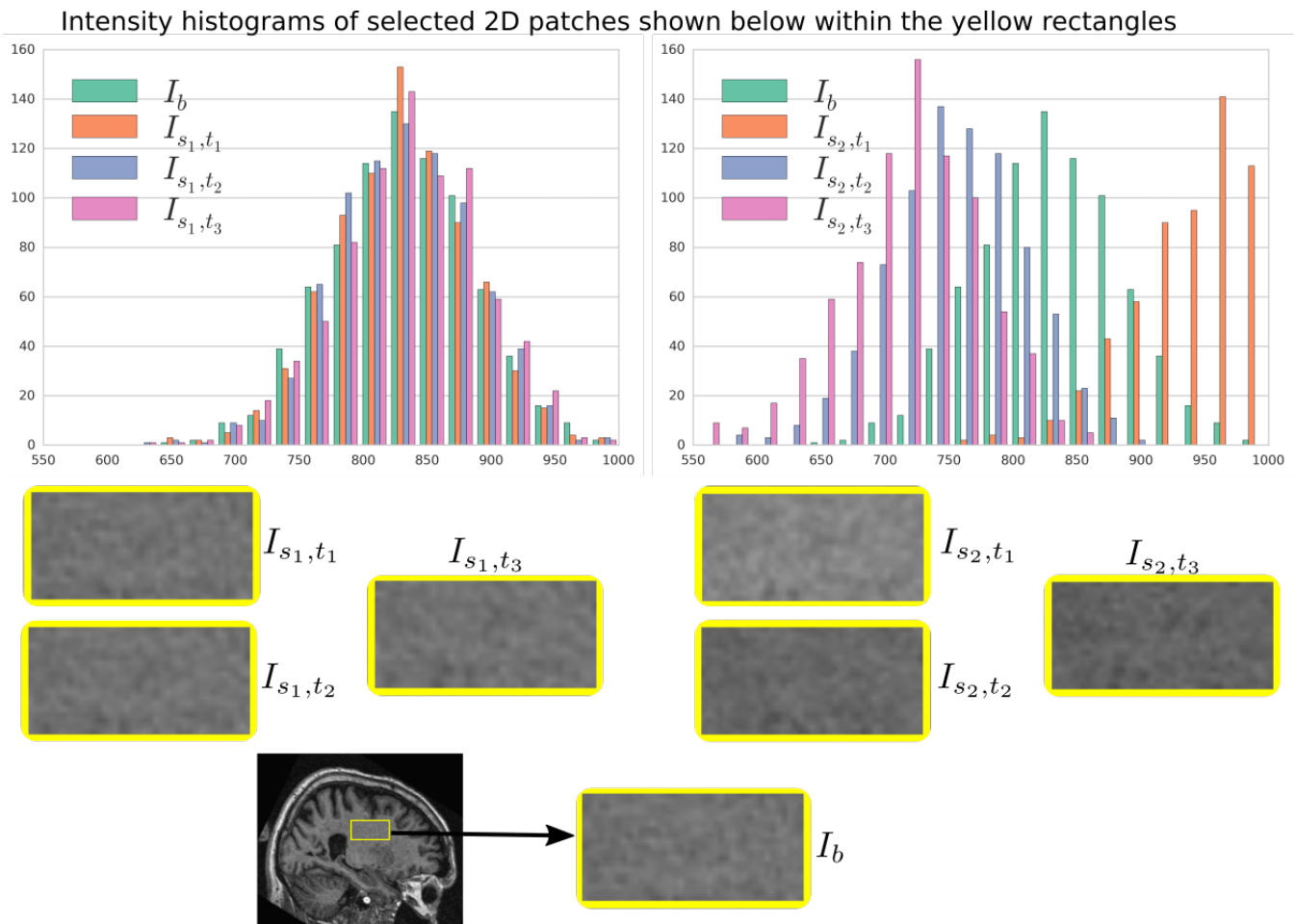


Figure 7. Intensity histograms of selected patches of the images simulated in Figure 6. When the simulated images are resampled from the same input baseline image I_b , as expected, the histograms of the simulated images closely match with each other. However, when simulated images are resampled from other different images of the same patients, the histograms of these simulated images do not match closely. The longitudinal sequence of simulated images I_{s_2,t_1} , I_{s_2,t_2} and I_{s_2,t_3} has realistic variation in intensities as observed in the real sequences.

277 In Figure 9, we show an example where synthetic sequence of images is simulated by starting from a
 278 baseline image of a healthy subject. However, the prescribed atrophy is derived from an atrophy estimated
 279 from the AD patient used in Figure 6. The input baseline images of both the AD patient and the healthy
 280 subject were segmented using FreeSurfer (Fischl et al., 2002). In all the segmented regions including the
 281 white matter parcellations of the AD patient, the average values of the smoothly varying atrophy map
 282 were computed. These regional average values of the atrophy computed from the AD patient were then
 283 transported to the corresponding regions of the healthy subject. Thus, in Figure 9, we can see that the
 284 prescribed atrophy is region-wise uniform instead of smoothly varying. For comparison, the figure also
 285 shows three real time-point images of the healthy subject along with the three simulated time-point images
 286 with atrophy derived from the AD patient.

4 SIMUL@TROPHY: CHOICES AVAILABLE AND PRACTICAL CONSIDERATIONS

287 Simul@tropy is available as an open-source repository under git version control. Researchers can use
 288 it according to their needs, improve the presented model, and/or add new models of brain atrophy. It is

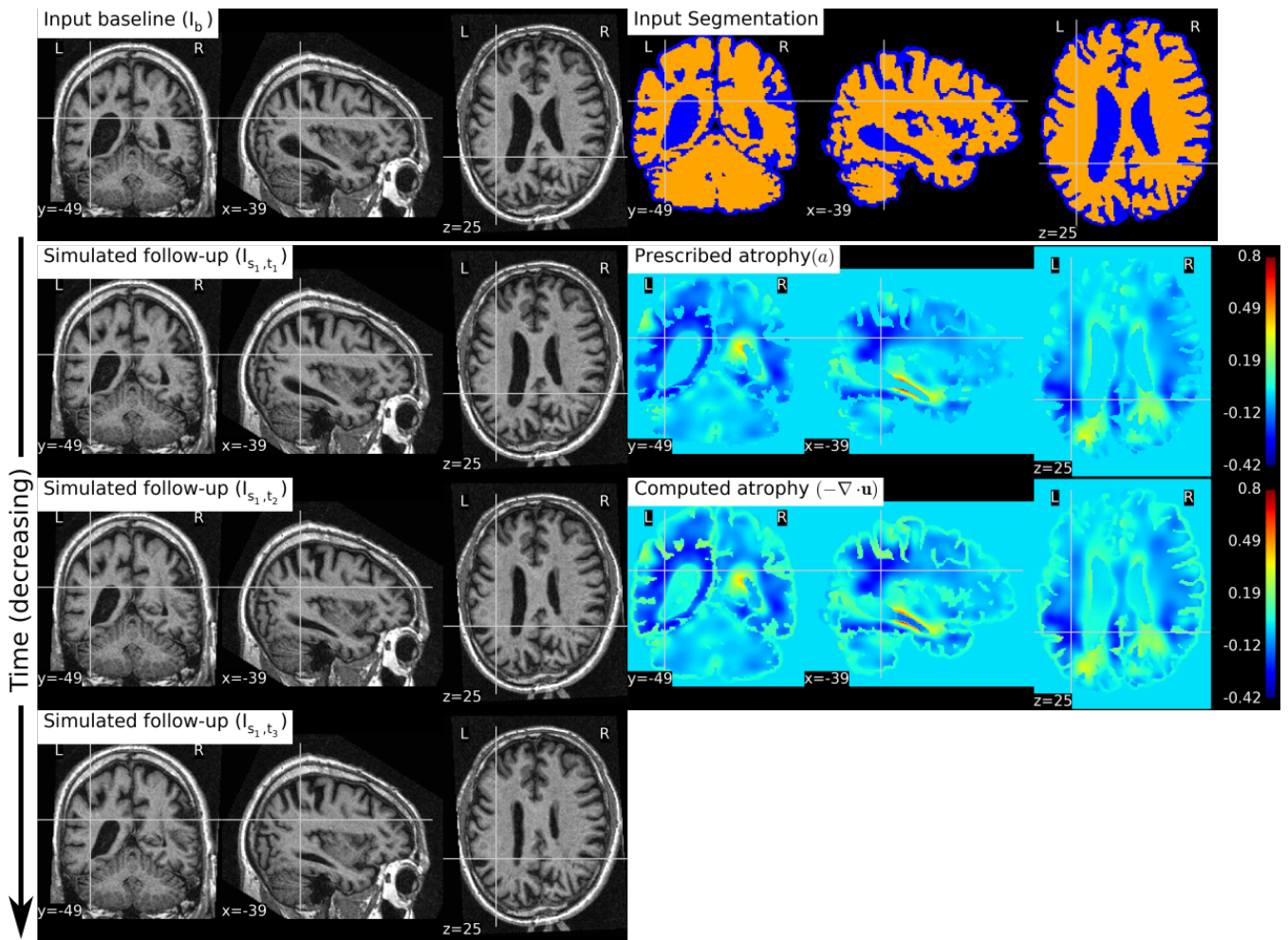


Figure 8. The figure shows an example of simulating a longitudinal sequence with backward time-points. The input baseline image I_b is the same one as used in Figure 6, and the prescribed atrophy map is the negative of the map used in Figure 6. In the figure, we can see the shrinkage of the ventricles and the growth of the brain parenchyma.

289 based on two core components: i) The Insight ToolKit (ITK) and ii) PETSc Balay et al. (2013). All the
 290 input and output images of the brain deformation model shown in Figure 1 can be in any format that ITK
 291 supports. ITK has strongly promoted reproducible science in the medical imaging domain, and has been
 292 widely used in computational science applied to medical imaging (McCormick et al., 2014; Avants et al.,
 293 2015). Similarly, implementation of the model solver is based on open-source PETSc, a library based on C
 294 programming language. It has also been very widely used in a very diverse set of applications that also
 295 include the medical field. It is a very powerful library that supports wide range of iterative solvers and
 296 preconditioners for large systems of equations. The solvers implemented in PETSc can scale very well to
 297 large distributive computer systems.

298 `Simul@trophy` runs from command lines where the required inputs and optional choices are provided
 299 via command line arguments. The available command lines are detailed in Appendix 7. In this section, we
 300 illustrate some examples of how certain choices made during the simulation affect output results.

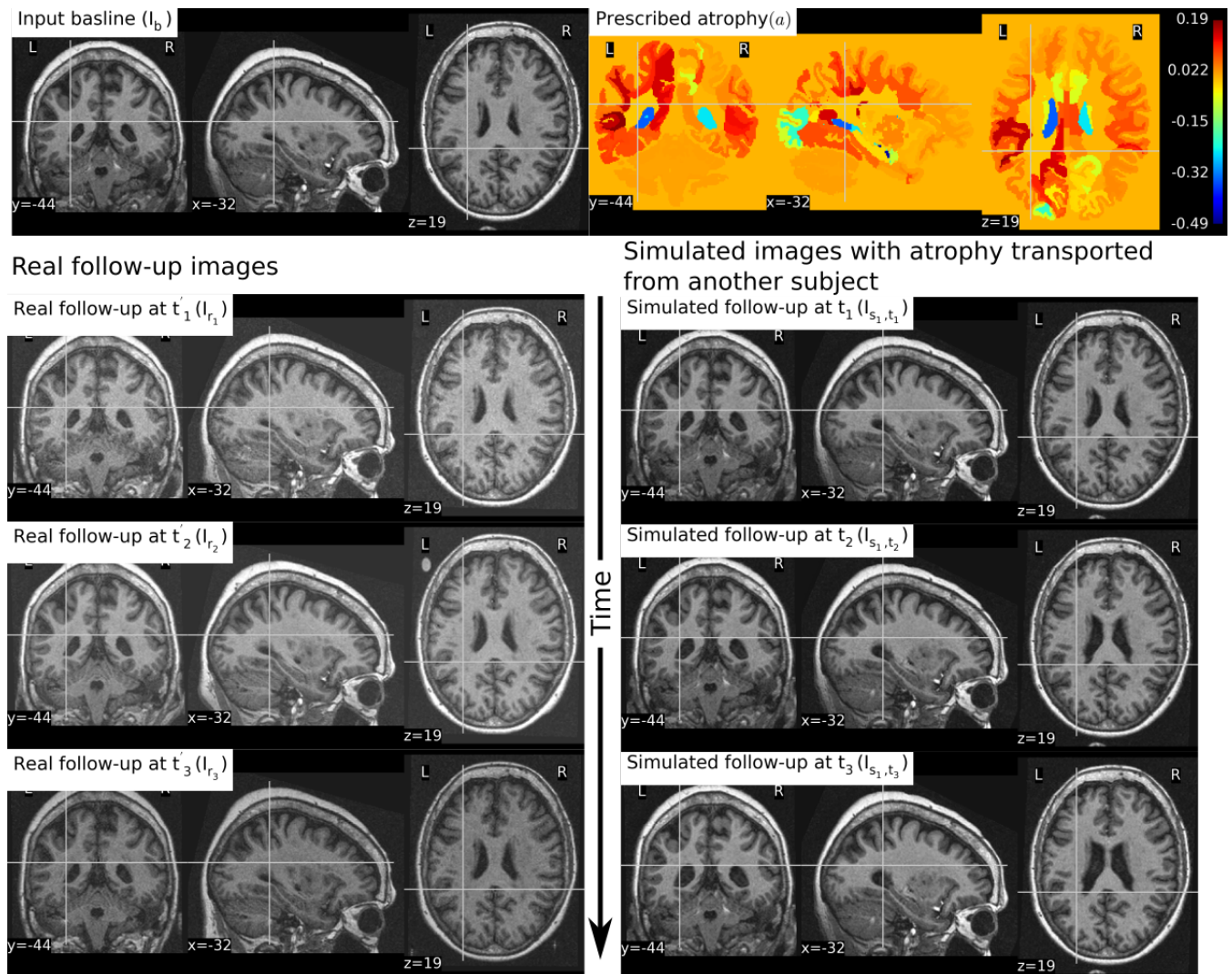


Figure 9. The figure shows an example of simulating follow-up images of a normal subject with baseline image I_b , where the prescribed atrophy pattern is adapted from an AD patient. The prescribed atrophy is adapted from the atrophy estimated for the AD patient shown in Figure 6. Average values of the smoothly varying prescribed atrophy shown in Figure 6 is computed in all the ROIs. The ROIs are obtained from the FreeSurfer segmentation including all the white matter parcellations (Fischl et al., 2002). The simulated images on the right have bigger shrinkage of the brain parenchyma and bigger expansion of the ventricles than the real images on the left.

301 **4.1 Impact of registration on simulated images**

302 In Section 2.3, we explained that starting from an input baseline image of a subject, I_b , we can generate
 303 two synthetic images:

$$I_{s1} = \Phi_{sim} \star I_f \quad \text{and} \quad I_{s2} = (\Phi_{sim} \circ \Phi_{reg}) \star I_f$$

304 where Φ_{sim} is the deformation field obtained from the brain deformation model using I_b as the input
 305 baseline image, and Φ_{reg} is the deformation field obtained from the non-rigid registration between I_b and a
 306 real follow-up image I_f . Perfect alignment of the two images with a non-rigid registration is possible only
 307 in the ideal case scenario. In such an ideal case, the simulated images I_{s1} and I_{s2} have identical shapes of
 308 the brain structures with the only differences lying in the intensity characteristics. In practice, this is almost

309 never the case, and we present below an example of the impact of registration result on the simulated
 310 images.

311 Let us use the following short notations for various images described in this section.

- 312 • RB: Real baseline image: I_b
- 313 • RF: Real follow-up image: I_f
- 314 • RB_to_RF: Real baseline aligned to real follow-up: $\Phi_{\text{reg}}^{-1} \star I_b$
- 315 • SF_in_RB: Simulated follow-up image with intensity resampled from I_b : $\Phi_s \star I_b$
- 316 • SF_in_RF: Simulated follow-up image with intensity resampled from I_f : $(\Phi_s \circ \Phi_{\text{reg}}) \star I_f$

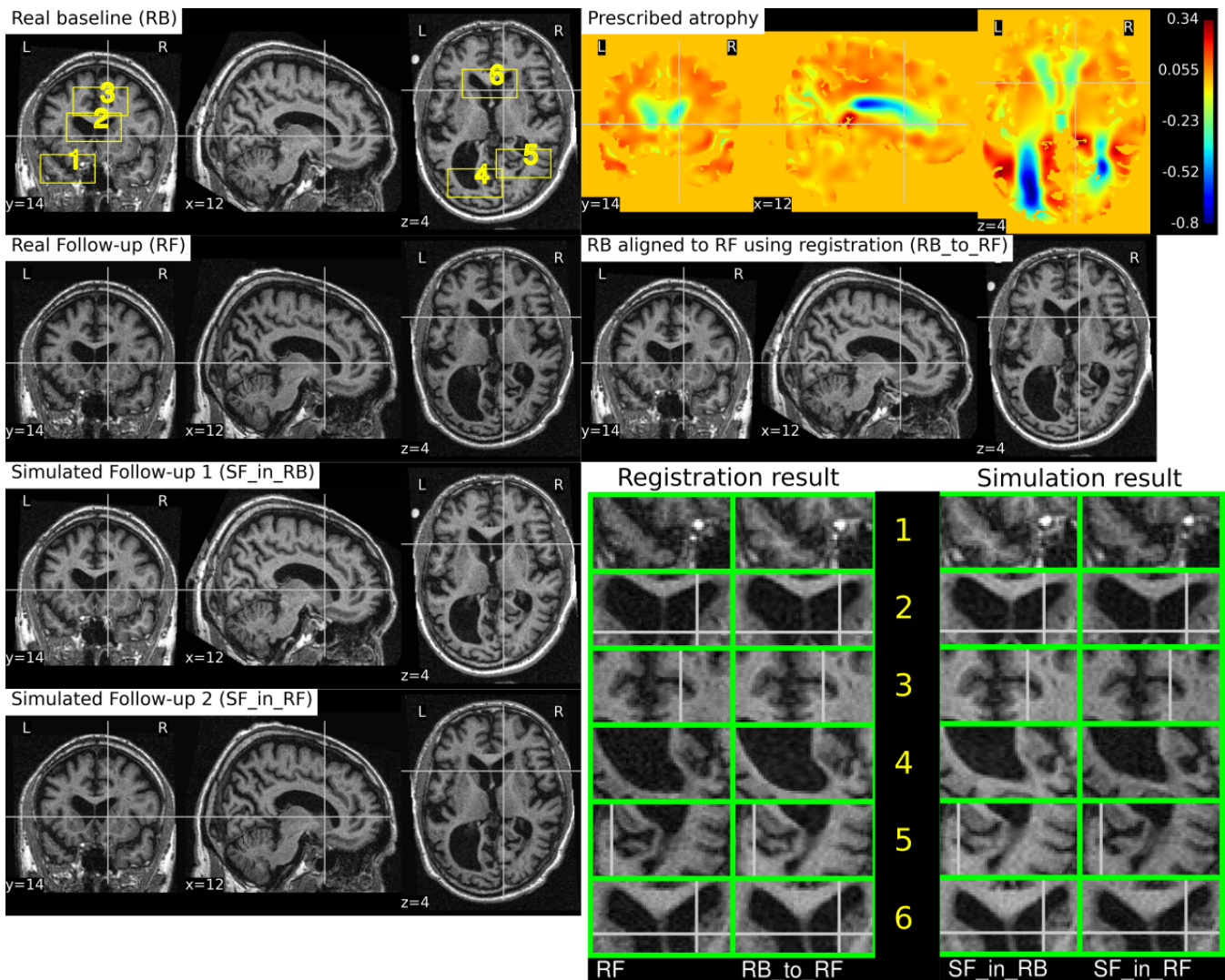


Figure 10. RB and RF are non-rigidly registered and the transformation obtained from the registration is used to align RB to RF which is shown in the image RB_to_RF. The figure also shows two simulated follow-up images SF_in_RB and SF_in_RF that are resampled from (RB) and (RF) respectively. We can see that in most regions of the brain, the two simulated images have almost identical morphological appearances. However, there are also regions such as 2 and 5, where the morphological appearances of the two simulated images are not identical. From the registration results for these regions 2 and 5 in the zoomed patches, we can see that the registration is also not accurate in those regions.

317 Figure 10 illustrates the impact of registration result Φ_{reg} on the simulation results. The figure shows
 318 both the registration and simulation results along with zoomed patches of RB, RB_to_RF, SF_in_RB
 319 and SF_in_RF. As expected, SF_in_RB and SF_in_RF have different intensity characteristics coming
 320 from RB and RF respectively. In the regions where registration is accurate, the two simulated images look
 321 almost identical except for the differences in the intensity characteristics. However, in the regions where
 322 registration is not accurate enough, SF_in_RB and SF_in_RF do not have identical shapes as expected.
 323 Thus, for the proposed method of using deformations obtained by registration for simulation, it might be
 324 preferable to use aggressive non-linear registrations with a much bigger weight given to similarity terms
 325 than the regularization terms.

326 4.2 Discretization scheme for the divergence computation

327 In Khanal et al. (2016b), a standard staggered grid discretization was used for solving the system of Eqs.
 328 (1). The discretization scheme is shown in Figure 11 in 2D for illustration; explanation on 2D extends
 329 naturally to 3D. In the figure, we can see that the components of the displacement field variable \mathbf{u} lie on
 330 cell faces and not at cell centres. However, all the input and output images for the model, including the
 331 output displacement field image, are standard images that have their values lying in cell centres or voxels.
 332 Our implementation of the solver internally creates the required staggered grid for the given input images.
 333 Once \mathbf{u} is computed within the solver of system of Eqs.(1), its values at cell faces are interpolated to obtain
 334 the values at cell centres which are then assembled to send as output displacement field image. Within the
 335 solver, the numerical scheme used for the discretization of $\nabla \cdot \mathbf{u} = -a$ is:

$$\frac{u_{i+1/2,j,k} - u_{i-1/2,j,k}}{h_x} + \frac{v_{i,j+1/2,k} - v_{i,j-1/2,k}}{h_y} + \frac{w_{i,j,k+1/2} - w_{i,j,k-1/2}}{h_z} = a_{i,j,k} \quad (2)$$

336 where,

$$\mathbf{u} = \begin{pmatrix} u \\ v \\ w \end{pmatrix}.$$

337 Simul@trophY then provides output displacement field image with the values of \mathbf{u} lying at cell centres
 338 or voxels by using linear interpolation as follows:

$$\begin{pmatrix} u_{i,j,k} \\ v_{i,j,k} \\ w_{i,j,k} \end{pmatrix} = \begin{pmatrix} (u_{i+1/2,j,k} + u_{i-1/2,j,k}) / 2 \\ (v_{i,j+1/2,k} + v_{i,j-1/2,k}) / 2 \\ (w_{i,j,k+1/2} + w_{i,j,k-1/2}) / 2 \end{pmatrix} \quad (3)$$

339 To compare divergence maps of this output field with the ones obtained from tools external of
 340 Simul@trophY, the only accessible values are the interpolated ones. ITK is widely used in registration
 341 based brain morphometry algorithms, but the default derivative computation of ITK has the following
 342 centred difference stencil:

$$\frac{u_{i+1,j,k} - u_{i-1,j,k}}{2 * h_x} + \frac{v_{i,j+1,k} - v_{i,j-1,k}}{2 * h_y} + \frac{w_{i,j,k+1} - w_{i,j,k-1}}{2 * h_z} = a_{i,j,k} \quad (4)$$

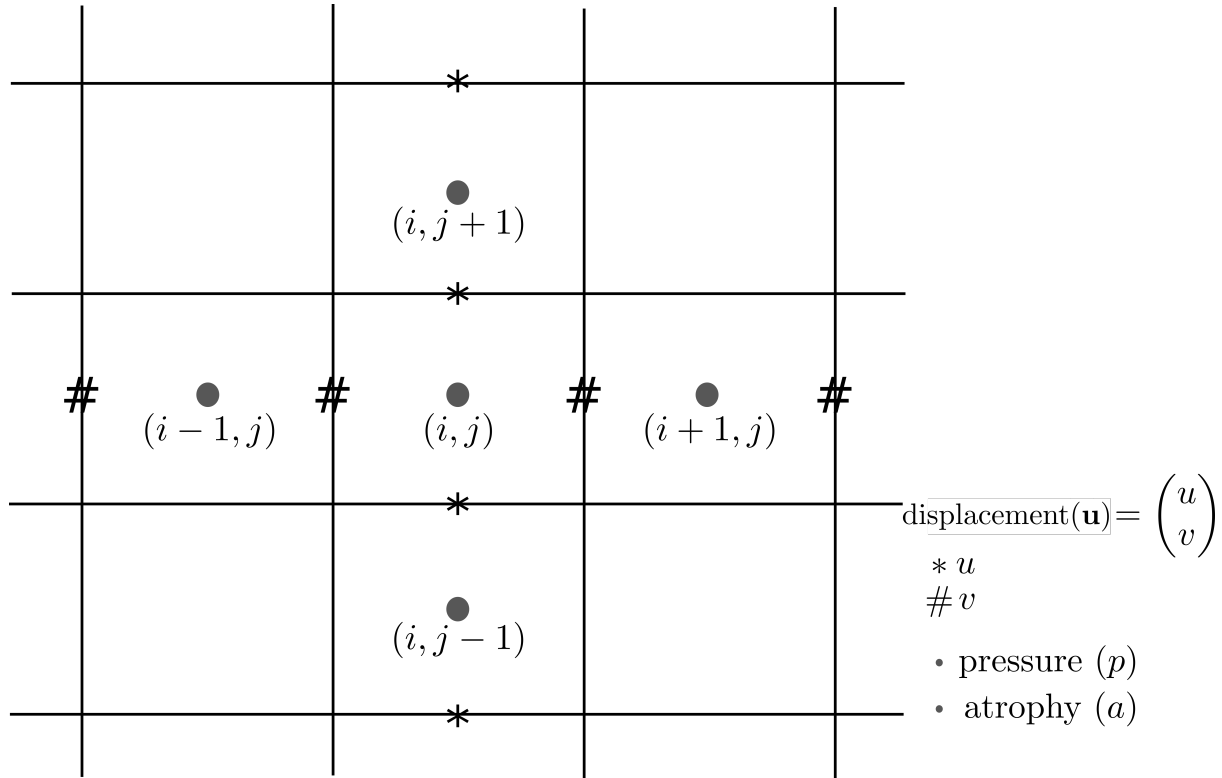


Figure 11. Standard staggered grid discretization scheme that is used to solve the system of Eqs. (1). Displacement variables are at faces (edges in 2D) of the cells, while pressure and atrophy values are at centres of the cells.

343 Replacing the components of \mathbf{u} at cell centres from Eq. 3, we get,

$$\frac{u_{i+3/2,j,k} + u_{i+1/2,j,k} - (u_{i-1/2,j,k} + u_{i+3/2,j,k})}{4 * h_x} + \dots = a_{i,j,k} \quad (5)$$

344 The scheme in Eq. (5) does not match the one that was used internally by `Simul@trophy` shown in
 345 Eq. (2). This results in discrepancy if we compare input prescribed atrophy maps against the externally
 346 computed divergence maps $\nabla \cdot \mathbf{u}$. Thus, in this work, we have added an implementation for the scheme
 347 in Eq. (5) so that users can choose either of the two possible schemes of Eq. (2) and Eq. (5). The latter
 348 scheme is consistent with the divergence computed by the default derivative computation options of ITK.
 349 At each 3D cell, the scheme in Eq. (2) involves 6 variables of the displacement field, while the scheme in
 350 Eq. (5) involves 12 variables. In the rest of the paper, they will be referred to as 6-point and 12-point
 351 schemes respectively.

352 Figure 12 shows the error in specified vs. obtained atrophy when using the two different numerical
 353 schemes. As expected, we can see that when a consistent numerical scheme is used, there is no difference
 354 between the specified and obtained atrophy. When the schemes are not consistent, the error is larger on the
 355 areas where the prescribed atrophy values change sharply.

356 If the simulated ground truth images using `Simul@trophy` are used for the evaluation of atrophy
 357 estimation algorithms, one must also be careful about the measure of volume change used in addition to
 358 the numerical scheme used. For instance, many TBM based brain morphometry algorithms use Jacobian
 359 determinants as a measure of volume change. To compute ground truth volume changes of the simulated

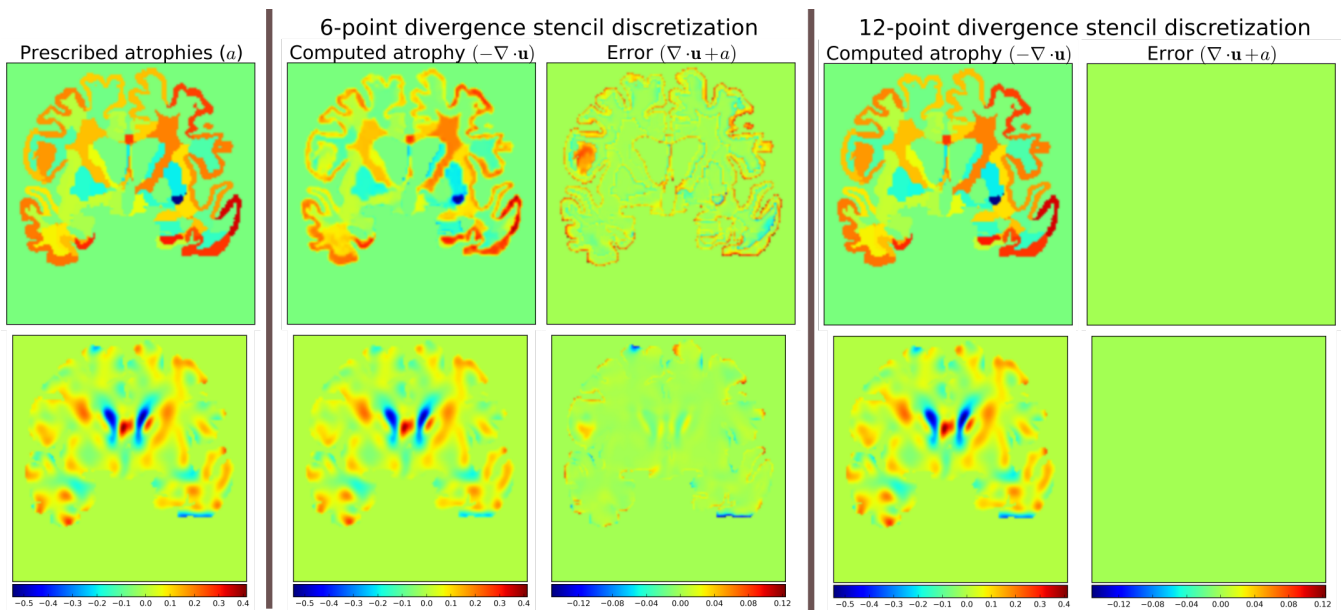


Figure 12. Error due to non-consistent numerical schemes in Eq. (2), and Eqs. (4 and 5). $\nabla \cdot \mathbf{u}$ shown in the figure are computed external of `Simul@troph` by using the default ITK derivative computation scheme shown in Eq. (4). When this divergence computation is consistent with the one used in `Simul@troph`, we should obtain zero error with $\nabla \cdot \mathbf{u} + a = 0$. This is indeed the case, as seen on the right, when we use 12-point stencil of Eq. 5. We see non-zero errors when using 6-point stencil from Eq. (2) because this scheme and the default ITK scheme are not consistent. The figure shows that the error gets larger at areas where prescribed atrophy has discontinuous jumps.

360 images for the evaluation of such algorithms, users should compute Jacobian determinants using the same
 361 numerical scheme as used by the atrophy estimation algorithm being evaluated. For instance, if multiple
 362 time-steps was used in simulating the final image then the Jacobian must be computed at each individual
 363 step and properly accumulated to get the final volume change.

364 4.3 Implementation of image warping

365 When implementing an algorithm to warp an image with a given deformation field, it is more convenient
 366 to use the inverse of the deformation field. If Φ_s is the output deformation field obtained from the brain
 367 deformation model by using I_b as the input baseline image, Φ_s maps any point \mathbf{x} in I_b to a point \mathbf{y} in the
 368 simulated image I_s as follows:

$$\mathbf{y} = \Phi_s(\mathbf{x}).$$

369 However, \mathbf{y} is not guaranteed to be a discrete voxel location. Since we do not know the intensity values
 370 of I_s *a priori* in the nearby discrete positions, the problem of interpolation is much more complex. Thus,
 371 we start from a discrete voxel location \mathbf{y} in I_s where the value of intensity is to be found. Then, the
 372 corresponding position \mathbf{x} in I_b can be obtained by using the inverse deformation field:

$$\mathbf{x} = \Phi_s^{-1}(\mathbf{y}).$$

373 If the transformed point \mathbf{x} is not a discrete point, we can interpolate the intensities of I_b from neighbouring
 374 discrete locations. Let us denote the interpolation by square brackets. Thus $i = I[\mathbf{x}]$ describes a mapping
 375 of a point \mathbf{x} to an intensity, i , of the MR image I at \mathbf{x} . Using this notation, the intensity of the simulated

376 image at any position \mathbf{x} is given by:

$$I_b [\Phi_s^{-1}(\mathbf{x})].$$

377 The following option can be used to invert the deformation field:

```
378 --invert_field_to_warp #Invert u; default: do not invert
```

381 The implementation of the inversion is adapted from a fixed-point scheme implementation available in
 382 ITK (Luethi, 2010). By default, the simulator uses B-spline interpolation of order three to warp the input
 383 images.

384 4.4 Standalone utility tools and scripts for pre-processing and post-processing

385 There are some standalone tools and scripts available for various pre-processing and post-processing
 386 operations that are detailed in the documentation of the released software.

387 Some of these tools for pre-processing and post-processing operations are C++ executables based on ITK,
 388 while others are python scripts. In this work, all the input segmentation of the model were obtained by using
 389 FreeSurfer. As explained in Khanal et al. (2016b), these segmentation maps were processed to obtain in the
 390 format required by the model. Although the provided scripts are developed for FreeSurfer segmentation
 391 maps, they can be easily modified to adapt to other pre-processing tools. Finally, the registration and
 392 simulation deformations were composed using `ComposeMultiTransform` of Advanced Neuroimaging
 393 Tools (ANTs) (Avants et al., 2011).

394 The core component of `Simul@trophy` is the implementation of the brain deformation model.
 395 Resampling of the intensity is straightforward once the deformations from the model and from registration
 396 are available. The simulator is not dependent on any one particular registration algorithm. Although we
 397 used LCC-LogDemons for illustrative purposes, this can be replaced with any other non-rigid registration
 398 algorithms. Similarly pre-processing is also independent of `Simul@trophy`. We used FreeSurfer in the
 399 simulation examples shown in this work, but any other skull stripping and segmentation algorithms can be
 400 used. `Simul@trophy` provides some example scripts and some utility scripts, which could be modified
 401 when using other tools for the pre-processing step.

5 DISCUSSION

402 In Khanal et al. (2016b), we presented a method to generate a subject-specific atrophy pattern by first
 403 measuring the atrophy from the available time-points, and then simulating a new time-point by prescribing
 404 the measured atrophy. In Khanal et al. (2016c), we extended the method to interpolate an unavailable
 405 intermediate time-point MRI. In this work, we added realistic variation in the intensity of the synthetic
 406 images. This fills an important gap in the existing literature to simulate atrophy in longitudinal images with
 407 realistic intensity variation without explicitly modeling the noise and acquisition artefacts. The simulation
 408 examples were shown using three types of atrophy patterns: i) very simple uniform volume changes in
 409 small number of regions, ii) uniform atrophy in large number of regions, and iii) smoothly varying atrophy
 410 patterns.

411 For each subject, we could generate large number of synthetic images by perturbing these atrophy patterns
 412 in different ways. Even with the same atrophy pattern, we can generate multiple sets of longitudinal
 413 sequences of varying intensity characteristics using the approach illustrated in Figure 4. Thus, by changing
 414 the atrophy patterns and the image intensities, `Simul@trophy` could be used to generate a database of

415 very large number of simulated images. Such a database might be useful for training of machine learning
416 algorithms.

417 In Figure 6, smoothly varying atrophy pattern was prescribed by taking the negative of the divergence of
418 a stationary velocity field obtained by registering the input baseline image with a follow-up image of the
419 same subject. The objective of the experiment was to illustrate the ability of *Simul@tropy* to simulate
420 smoothly varying patterns of atrophy in addition to the piecewise continuous atrophy maps. Registration
421 was taken just as a means of getting a realistic smoothly varying atrophy maps; it is worth mentioning that
422 simulating the deformation to be close to the deformation obtained from the registration algorithm was not
423 the objective of this experiment. This is because the actual deformation field depends on the regularization
424 used in the registration algorithm which does not necessarily follow the modeling assumptions used by
425 *Simul@tropy*.

426 Although the proposed method of resampling intensity from an image different from the input image
427 provides more realistic variations, there are nevertheless certain issues one needs to be aware of. Since the
428 simulated image has its intensities interpolated from another image, it can slightly reduce the noise variance.
429 A neighbourhood with expansion in the simulated image have intensities with slightly different linear
430 combinations of intensities coming from a smaller set of voxels in the input image. Thus, the simulated
431 image would have a smoother autocorrelation in the neighbourhood compared to an equivalent real image.
432 The fact that the simulated image has undergone interpolation and draws intensities from a limited set of
433 raw voxels means that it is inherently smoother than the real scans. Finally, the usual spatial patterns of
434 artifacts on real scans might not be exactly reproduced when warping real images. Any application using
435 the simulated sets of images with the proposed approach should be aware of and ideally take into account
436 these issues when interpreting results.

437 Use of repeat baseline scans to obtain intensity variation in the simulated images provides a very simple
438 approach without using explicit noise and artifact models. One limitation with this is that the repeat baseline
439 scans are not always available. When repeat scans are not available, we have proposed to use images at
440 other time-points of the same subject, which requires performing non-linear registration. However, none
441 of the non-linear registration methods are perfect and therefore the inaccuracies in registration affect the
442 simulation results. This issue was discussed with illustrative examples in Section 4.1.

443 *Simul@tropy* can be used in evaluating atrophy estimation algorithms in similar ways as done by
444 Pieperhoff et al. (2008); Camara et al. (2008); Sharma et al. (2010). Since the proposed approach to
445 simulate images may need deformations estimated from image registration, the use of these simulated
446 images for the evaluation of some registration algorithms can bring an issue of circularity. This limitation
447 adds to another limitation present in all publications related to atrophy simulation that we are aware of:
448 namely, the models used in simulating images could favour certain kinds of registration algorithms over
449 others. Although the ground truth atrophy can be measured from the combined deformation fields, the
450 users must be aware of both limitations when they use *Simul@tropy* for the evaluation of registration
451 algorithms.

452 The ability to prescribe atrophy at any time point allows the user to introduce volume changes at different
453 regions of the brain at different times. Thus, another interesting application of the simulator is to train
454 and/or validate disease progression models such as the models proposed in Chen et al. (2012); Fonteijn
455 et al. (2012); Jedynek et al. (2012); Dukart et al. (2013); Schmidt-Richberg et al. (2016). Having a database
456 of longitudinal MRIs with known spatio-temporal distribution of atrophy can be useful to validate such

457 algorithms. Furthermore, since the algorithms use a data driven approach, the simulator could be useful to
458 train or fine-tune such models.

459 Another possible application is in filling up unavailable time-point MRIs of some of the subjects, when
460 performing group-wise longitudinal analysis. In such studies, usually the available time-point images of
461 each subject are used to estimate subject-specific volume changes. These subject-specific measurements
462 are then used to perform group-wise statistics to check whether there are significant differences amongst
463 different groups in some particular regions of the brain. Databases used in such analyses, might not always
464 have all the required time-point images for all the subjects. This could lead to bias if all the subjects are not
465 aligned properly in the temporal dimension of disease progression. Simulating new time-point images for
466 some subjects and using them in the analysis might allow evaluating the impact of such mis-alignments.

467 `Simul@tropy` could also be used in studying the role of morphology and intensity on atrophy
468 estimation algorithms, and in machine learning based AD classification algorithms. `Simul@tropy`
469 enables to perform such studies as it allows creating a large number of images by simulating atrophy
470 patterns commonly observed in AD patients but with intensities taken from normal subjects and vice versa.

471 We hope to promote two directions of research in the community with open-source release of
472 `Simul@tropy`. *First*, the public availability of `Simul@tropy` enables researchers to build their own
473 simulated databases as needed. This might also hopefully lead to a large public database of ground truth
474 simulated images, that could be used for benchmarking and evaluation of various image based morphometry
475 tools. *Second*, we hope that `Simul@tropy` allows other researchers to build upon the biophysical model
476 we presented in Khanal et al. (2016b), and investigate further, providing more accurate models of brain
477 atrophy.

478 Finally, `Simul@tropy` is general enough to be used for other imaging modalities such as CT scans.
479 It could also be used with images of any other organs, where one requires simulating specified volume
480 changes. In this case, the pre-processing should be changed accordingly to generate a segmentation image
481 and atrophy maps. Thus, once the software is public, other researchers might find it useful in applications
482 that we have not foreseen yet.

6 CONCLUSIONS

483 We proposed a simulation framework that can generate realistic longitudinal MRIs with specified volume
484 changes. The framework allows generating large number of subject-specific multiple time-point images
485 based on a biophysical model of brain deformation due to atrophy. We developed an open-source software
486 `Simul@tropy` to implement the proposed framework. The core part of `Simul@tropy` is the
487 implementation of our brain deformation model presented in Khanal et al. (2016b). `Simul@tropy` is
488 based on widely used state of the art libraries PETSc (for solving large systems of equations) and ITK (for
489 medical image processing). Since the software is publicly available in an open-source repository, we hope
490 that researchers can use it to create databases of ground truth images. The framework could be used to
491 generate a common public database, which in turn could be used to validate and evaluate a large number
492 of available atrophy estimation algorithms. Similarly, these databases could be valuable for data driven
493 disease progression models including machine learning algorithms. Validation and training of the models
494 that study temporal relationships, ordering and co-evolution of atrophy in different structures of the brain
495 could be another interesting application.

CONFLICT OF INTEREST STATEMENT

496 The authors declare that the research was conducted in the absence of any commercial or financial
497 relationships that could be construed as a potential conflict of interest.

FUNDING

498 Part of this work was funded by the European Research Council through the ERC Advanced Grant
499 MedYMA 2011-291080.

ACKNOWLEDGMENTS

500 1. We would like to thank Mehdi Hadj-Hamou for providing us registration results and the associated
501 deformation fields that were used in this paper to resample intensity from different images. The
502 preprocessing steps involved for this registration are explained in Hadj-Hamou et al. (2016).
503 2. Most part of this work has first appeared in the PhD thesis of Bishesh Khanal (Khanal, 2016), and the
504 working paper has been archived (Khanal et al., 2016a).
505 3. Part of this work was funded by the European Research Council through the ERC Advanced Grant
506 MedYMA 2011-291080.
507 4. This work benefited from the use of the Insight Segmentation and Registration Toolkit (ITK), an open
508 source software developed as an initiative of the U.S. National Library of Medicine and available at
509 www.itk.org.
510 5. The multi-platform configuration tool CMake was used for configuring ITK and facilitating its use from
511 our project. CMake was partially funded by the U.S. National Library of Medicine as part of the Insight
512 Toolkit project. CMake is an open source system and it is freely available at www.cmake.org.

SUPPLEMENTAL DATA

513 Supplementary Material should be uploaded separately on submission, if there are Supplementary Figures,
514 please include the caption in the same file as the figure. LaTeX Supplementary Material templates can be
515 found in the Frontiers LaTeX folder

REFERENCES

- 516 Ashburner, J. (2013). Symmetric diffeomorphic modeling of longitudinal structural MRI. *Frontiers in*
517 *Neuroscience* 6. doi:10.3389/fnins.2012.00197
- 518 Ashburner, J. and Friston, K. J. (2000). Voxel-based morphometry: the methods. *NeuroImage* 11, 805 – 821.
519 doi:10.1006/nimg.2000.0582
- 520 Ashburner, J. and Ridgway, G. R. (2015). Tensor-based morphometry. In *Brain Mapping: An Encyclopedic*
521 *Reference*, ed. A. W. Toga (Academic Press: Elsevier). 383–394. doi:10.1016/B978-0-12-397025-1.
522 00309-2
- 523 Avants, B., Johnson, H. J., and Tustison, N. J. (2015). Neuroinformatics and the the insight toolkit.
524 *Frontiers in Neuroinformatics* 9. doi:10.3389/fninf.2015.00005
- 525 Avants, B. B., Tustison, N. J., Song, G., Cook, P. A., Klein, A., and Gee, J. C. (2011). A reproducible
526 evaluation of ants similarity metric performance in brain image registration. *NeuroImage* 54, 2033 –
527 2044. doi:<http://dx.doi.org/10.1016/j.neuroimage.2010.09.025>

- 528 Balay, S., Brown, J., Buschelman, K., Gropp, W. D., Kaushik, D., Knepley, M. G., et al. (2013). PETSc
529 Web page. [Http://www.mcs.anl.gov/petsc](http://www.mcs.anl.gov/petsc)
- 530 Camara, O., Schnabel, J. A., Ridgway, G. R., Crum, W. R., Douiri, A., Scahill, R. I., et al. (2008). Accuracy
531 assessment of global and local atrophy measurement techniques with realistic simulated longitudinal
532 alzheimer's disease images. *NeuroImage* 42, 696–709
- 533 Camara, O., Schweiger, M., Scahill, R. I., Crum, W. R., Sneller, B. I., Schnabel, J. A., et al. (2006).
534 Phenomenological model of diffuse global and regional atrophy using finite-element methods. *IEEE*
535 *Transactions on Medical Imaging* 25, 1417–30. doi:10.1109/TMI.2006.880588
- 536 Camara-Rey, O., Sneller, B. I., Ridgway, G. R., Garde, E., Fox, N. C., and Hill, D. L. (2006). Simulation
537 of acquisition artefacts in mr scans: effects on automatic measures of brain atrophy. In *International*
538 *Conference on Medical Image Computing and Computer-Assisted Intervention* (Springer), 272–280
- 539 Carmichael, O., McLaren, D. G., Tommet, D., Mungas, D., and Jones, R. N. (2013). Coevolution of brain
540 structures in amnesic mild cognitive impairment. *NeuroImage* 66, 449–456. doi:10.1016/j.neuroimage.
541 2012.10.029
- 542 Chen, R., Resnick, S. M., Davatzikos, C., and Herskovits, E. H. (2012). Dynamic bayesian network
543 modeling for longitudinal brain morphometry. *NeuroImage* 59, 2330 – 2338. doi:http://dx.doi.org/10.
544 1016/j.neuroimage.2011.09.023
- 545 Dukart, J., Kherif, F., Mueller, K., Adaszewski, S., Schroeter, M. L., Frackowiak, R. S. J., et al. (2013).
546 Generative fdg-pet and mri model of aging and disease progression in alzheimer's disease. *PLoS Comput*
547 *Biol* 9, 1–11. doi:10.1371/journal.pcbi.1002987
- 548 Fischl, B., Salat, D. H., Busa, E., Albert, M., Dieterich, M., Haselgrove, C., et al. (2002). Whole Brain
549 Segmentation: Automated Labeling of Neuroanatomical Structures in the Human Brain. *Neuron* 33,
550 341–355. doi:10.1016/S0896-6273(02)00569-X
- 551 Fonteijn, H. M., Modat, M., Clarkson, M. J., Barnes, J., Lehmann, M., Hobbs, N. Z., et al. (2012).
552 An event-based model for disease progression and its application in familial Alzheimer's disease and
553 Huntington's disease. *NeuroImage* 60, 1880–1889. doi:10.1016/j.neuroimage.2012.01.062
- 554 Freeborough, P. A. and Fox, N. C. (1997). The boundary shift integral: an accurate and robust measure
555 of cerebral volume changes from registered repeat mri. *IEEE Transactions on Medical Imaging* 16,
556 623–629. doi:10.1109/42.640753
- 557 Frisoni, G. B., Fox, N. C., Jack, C. R., Scheltens, P., and Thompson, P. M. (2010). The clinical use of
558 structural MRI in Alzheimer disease. *Nature Reviews. Neurology* 6, 67–77. doi:10.1038/nrneurol.2009.
559 215
- 560 Gorgolewski, K. J., Varoquaux, G., Rivera, G., Schwartz, Y., Ghosh, S. S., Maumet, C., et al. (2015).
561 Neurovault.org: A web-based repository for collecting and sharing unthresholded statistical maps of the
562 human brain. *Frontiers in Neuroinformatics* 9. doi:10.3389/fninf.2015.00008
- 563 Gudbjartsson, H. and Patz, S. (1995). The Rician Distribution of Noisy MRI Data. *Magnetic resonance*
564 *in medicine : official journal of the Society of Magnetic Resonance in Medicine / Society of Magnetic*
565 *Resonance in Medicine* 34, 910–914
- 566 Hadj-Hamou, M., Lorenzi, M., Ayache, N., and Pennec, X. (2016). Longitudinal analysis of image time
567 series with diffeomorphic deformations: a computational framework based on stationary velocity fields.
568 *Frontiers in Neuroscience* 10. doi:10.3389/fnins.2016.00236
- 569 Hua, X., Leow, A. D., Parikshak, N., Lee, S., Chiang, M.-C., Toga, A. W., et al. (2008). Tensor-based
570 morphometry as a neuroimaging biomarker for alzheimer's disease: An {MRI} study of 676 ad, mci, and
571 normal subjects. *NeuroImage* 43, 458 – 469. doi:http://dx.doi.org/10.1016/j.neuroimage.2008.07.013

- 572 Jedynak, B. M., Lang, A., Liu, B., Katz, E., Zhang, Y., Wyman, B. T., et al. (2012). A
573 computational neurodegenerative disease progression score: Method and results with the alzheimer's
574 disease neuroimaging initiative cohort. *NeuroImage* 63, 1478 – 1486. doi:http://dx.doi.org/10.1016/j.
575 neuroimage.2012.07.059
- 576 Jenkinson, M. and Smith, S. (2001). A global optimisation method for robust affine registration of brain
577 images. *Medical Image Analysis* 5, 143 – 156. doi:http://dx.doi.org/10.1016/S1361-8415(01)00036-6
- 578 Karaçali, B. and Davatzikos, C. (2006). Simulation of tissue atrophy using a topology preserving
579 transformation model. *IEEE Transactions on Medical Imaging* 25, 649–52. doi:10.1109/TMI.2006.
580 873221
- 581 Khanal, B. (2016). *Modeling and simulation of realistic longitudinal structural brain MRIs with atrophy in*
582 *Alzheimer's disease*. theses, Université Nice Sophia Antipolis
- 583 Khanal, B., Ayache, N., and Pennec, X. (2016a). Simulating Realistic Synthetic Longitudinal Brain MRIs
584 with known Volume Changes. Working paper or preprint
- 585 Khanal, B., Lorenzi, M., Ayache, N., and Pennec, X. (2014). A Biophysical Model of Shape Changes
586 due to Atrophy in the Brain with Alzheimers Disease. In *Medical Image Computing and Computer-*
587 *Assisted Intervention MICCAI 2014*, eds. P. Golland, N. Hata, C. Barillot, J. Hornegger, and R. Howe
588 (Springer International Publishing), vol. 8674 of *Lecture Notes in Computer Science*. 41–48. doi:10.
589 1007/978-3-319-10470-6_6
- 590 Khanal, B., Lorenzi, M., Ayache, N., and Pennec, X. (2016b). A biophysical model of brain deformation
591 to simulate and analyze longitudinal mris of patients with alzheimer's disease. *NeuroImage* 134, 35 – 52.
592 doi:http://dx.doi.org/10.1016/j.neuroimage.2016.03.061
- 593 Khanal, B., Lorenzi, M., Ayache, N., and Pennec, X. (2016c). Simulating patient specific multiple
594 time-point mris from a biophysical model of brain deformation in alzheimer's disease. In *Computational*
595 *Biomechanics for Medicine: Imaging, Modeling and Computing*, eds. G. Joldes, B. Doyle, A. Wittek,
596 P. M. F. Nielsen, and K. Miller (Springer International Publishing AG)
- 597 Koch, K., Reess, T. J., Rus, O. G., and Zimmer, C. (2016). Extensive learning is associated with gray
598 matter changes in the right hippocampus. *NeuroImage* 125, 627 – 632. doi:http://dx.doi.org/10.1016/j.
599 neuroimage.2015.10.056
- 600 Langlois, S., Desvignes, M., Constans, J. M., and Revenu, M. (1999). MRI geometric distortion: a simple
601 approach to correcting the effects of non-linear gradient fields. *Journal of magnetic resonance imaging:*
602 *JMRI* 9, 821–831
- 603 Lorenzi, M., Ayache, N., Frisoni, G., and Pennec, X. (2013). LCC-Demons: A robust and accurate
604 symmetric diffeomorphic registration algorithm. *NeuroImage* 81, 470–483. doi:10.1016/j.neuroimage.
605 2013.04.114
- 606 Luethi, M. (2010). Inverting deformation fields using a fixed point iteration scheme. *The Insight Journal*
- 607 Marcus, D. S., Fotenos, A. F., Csernansky, J. G., Morris, J. C., and Buckner, R. L. (2010). Open access
608 series of imaging studies: Longitudinal MRI data in nondemented and demented older adults. *Journal of*
609 *Cognitive Neuroscience* 22, 2677–2684
- 610 McCormick, M. M., Liu, X., Ibanez, L., Jomier, J., and Marion, C. (2014). Itk: Enabling reproducible
611 research and open science. *Frontiers in Neuroinformatics* 8. doi:10.3389/fninf.2014.00013
- 612 Modat, M., Simpson, I. J. A., Cardoso, M. J., Cash, D. M., Toussaint, N., Fox, N. C., et al. (2014).
613 Simulating neurodegeneration through longitudinal population analysis of structural and diffusion
614 weighted mri data. In *Medical Image Computing and Computer-Assisted Intervention – MICCAI 2014:*
615 *17th International Conference, Boston, MA, USA, September 14-18, 2014, Proceedings, Part III*, eds.

- 616 P. Golland, N. Hata, C. Barillot, J. Hornegger, and R. Howe (Springer International Publishing), Lecture
617 Notes in Computer Science. 57–64. doi:10.1007/978-3-319-10443-0_8
- 618 Pieperhoff, P., Südmeyer, M., Hömke, L., Zilles, K., Schnitzler, A., and Amunts, K. (2008). Detection
619 of structural changes of the human brain in longitudinally acquired MR images by deformation field
620 morphometry: methodological analysis, validation and application. *NeuroImage* 43, 269–87. doi:10.
621 1016/j.neuroimage.2008.07.031
- 622 Prados, F., Cardoso, M. J., Leung, K. K., Cash, D. M., Modat, M., Fox, N. C., et al. (2015). Measuring
623 brain atrophy with a generalized formulation of the boundary shift integral. *Neurobiology of aging* 36,
624 S81–S90
- 625 Prakosa, A., Sermesant, M., Delingette, H., Marchesseau, S., Saloux, E., Allain, P., et al. (2013). Generation
626 of synthetic but visually realistic time series of cardiac images combining a biophysical model and
627 clinical images. *IEEE transactions on medical imaging* 32, 99–109. doi:10.1109/TMI.2012.2220375
- 628 Preboske, G. M., Gunter, J. L., Ward, C. P., and Jack, C. R. (2006). Common mri acquisition non-idealities
629 significantly impact the output of the boundary shift integral method of measuring brain atrophy on
630 serial mri. *Neuroimage* 30, 1196–1202
- 631 Radua, J., Canales-Rodriguez, E. J., Pomarol-Clotet, E., and Salvador, R. (2014). Validity of modulation
632 and optimal settings for advanced voxel-based morphometry. *NeuroImage* 86, 81 – 90. doi:http:
633 //dx.doi.org/10.1016/j.neuroimage.2013.07.084
- 634 Rosen, H. J., Gorno-Tempini, M. L., Goldman, W., Perry, R., Schuff, N., Weiner, M., et al. (2002). Patterns
635 of brain atrophy in frontotemporal dementia and semantic dementia. *Neurology* 58, 198–208
- 636 Schmidt-Richberg, A., Ledig, C., Guerrero, R., Molina-Abril, H., Frangi, A., Rueckert, D., et al. (2016).
637 Learning biomarker models for progression estimation of alzheimer’s disease. *PLoS ONE* 11, 1–27.
638 doi:10.1371/journal.pone.0153040
- 639 Sepulcre, J., Sastre-Garriga, J., Cercignani, M., Ingle, G. T., Miller, D. H., and Thompson, A. J. (2006).
640 Regional gray matter atrophy in early primary progressive multiple sclerosis: a voxel-based morphometry
641 study. *Archives of neurology* 63, 1175–1180
- 642 Sharma, S., Noblet, V., Rousseau, F., Heitz, F., Rumbach, L., and Armspach, J. (2010). Evaluation of brain
643 atrophy estimation algorithms using simulated ground-truth data. *Medical Image Analysis* 14, 373–89.
644 doi:10.1016/j.media.2010.02.002
- 645 Sharma, S., Rousseau, F., Heitz, F., Rumbach, L., and Armspach, J. (2013). On the estimation and correction
646 of bias in local atrophy estimations using example atrophy simulations. *Computerized Medical Imaging
647 and Graphics* 37, 538 – 551. doi:http://dx.doi.org/10.1016/j.compmedimag.2013.07.002
- 648 Simmons, A., Tofts, P. S., Barker, G. J., and Arridge, S. R. (1994). Sources of intensity nonuniformity in
649 spin echo images at 1.5 t. *Magnetic Resonance in Medicine* 32, 121–128
- 650 Sled, J. G., Zijdenbos, A. P., and Evans, A. C. (1998). A nonparametric method for automatic correction of
651 intensity nonuniformity in MRI data. *IEEE transactions on medical imaging* 17, 87–97. doi:10.1109/42.
652 668698
- 653 Smith, A. D. C., Crum, W. R., Hill, D. L., Thacker, N. A., and Bromiley, P. A. (2003). Biomechanical
654 simulation of atrophy in MR images. In *Medical Imaging 2003* (International Society for Optics and
655 Photonics), 481–490
- 656 Smith, S. M., Zhang, Y., Jenkinson, M., Chen, J., Matthews, P., Federico, A., et al. (2002). Accurate,
657 robust, and automated longitudinal and cross-sectional brain change analysis. *Neuroimage* 17, 479–489
- 658 Whitwell, J. L. and Jack Jr, C. R. (2005). Comparisons between alzheimer disease, frontotemporal
659 lobar degeneration, and normal aging with brain mapping. *Topics in Magnetic Resonance Imaging* 16,
660 409–425

661 Wright, I., McGuire, P., Poline, J.-B., Travers, J., Murray, R., Frith, C., et al. (1995). A voxel-based method
 662 for the statistical analysis of gray and white matter density applied to schizophrenia. *NeuroImage* 2, 244
 663 – 252. doi:http://dx.doi.org/10.1006/nimg.1995.1032

7 APPENDIX

664 7.1 Running simul@tropy from command lines

665 Once the pre-processing steps described in Section 2.1 are performed and the desired atrophy map is
 666 generated, these images can be used as input to the model by providing the following command line
 667 arguments:

```
668 -atrophyFile          #Input atrophy map
669 -maskFile            #Input segmentation file
670 -imageFile           #Input image file
671
```

673 If the model parameters μ and λ have uniform values in Label1 and Label2, they can be provided
 674 as an argument to the option `-parameters`. On the other hand, if they need to have different values in
 675 different parts of the brain, one needs to provide them as images similar to other input images as shown
 676 below:

```
677 -parameters          # $\mu, \lambda$  in Region1, Region2. Format:  $\mu_1, \mu_2, \lambda_1, \lambda_2$ 
678 -muFile              #Ignore  $\mu$  from -parameters, use this image
679 -lambdaFile          #Ignore  $\lambda$  from -parameters, use this image
680 --useTensorLambda   # $\lambda$  given as DTI; default is scalar image
681
```

683 Some of the important options available are:

```
684 -boundary_condition #dirichlet_at_walls or dirichlet_at_skull
685 --div12pt_stencil  #Use 12-point scheme; default: 6-point scheme
686 --relax_ic_in_csf  #Region1:  $\nabla \cdot \mathbf{u} + kp = 0$ ; default is  $\nabla \cdot \mathbf{u} = -a$ 
687 -relax_ic_coeff     #Value of  $k$ 
688 -numOfTimeSteps    #Number of time-steps to solve for
689
```

691 To solve the system of Eqs. (1), the argument to `-boundary_condition` should be
 692 `dirichlet_at_skull` and `--relax_ic_in_csf` must be provided. Using `dirichlet_at_walls`
 693 instead of `dirichlet_at_skull` will consider regions with `label0` in the same way as the regions
 694 with `label2`, and sets the Dirichlet boundary conditions only at the image borders.

695 If `-numofTimeSteps` is greater than one, the simulator provides an output displacement field obtained
 696 by composing output displacement fields of each time-steps. For any time-step $n < \text{numOfTimeSteps}$,
 697 it also provides output synthetic image by warping the input image with the displacement field obtained by
 698 composing output displacement fields from time-step 1 to n . In addition to these outputs, if desired, some
 699 other extra outputs can be generated as shown below:

```
700 -resPath              #Result path to store all the results
701 -resultsFileNamesPrefix #Prefix to be provided to all the images
702 --writePressure       #Write  $p$  as image to disk.
703
```

```
704 --writeForce           #Write  $(\mu + \lambda)\nabla a$  as image to disk.  
705 --writeResidual       #Write solver residual as image to disk.  
706
```

FIGURES